

# Mixing Sauces: A Viscosity Blending Model for Shear Thinning Fluids

KENTARO NAGASAWA\*, The University of Tokyo

TAKAYUKI SUZUKI, The University of Tokyo

RYOHEI SETO, Kyoto University

MASATO OKADA, The University of Tokyo

YONGHAO YUE\*, The University of Tokyo, Aoyama Gakuin University

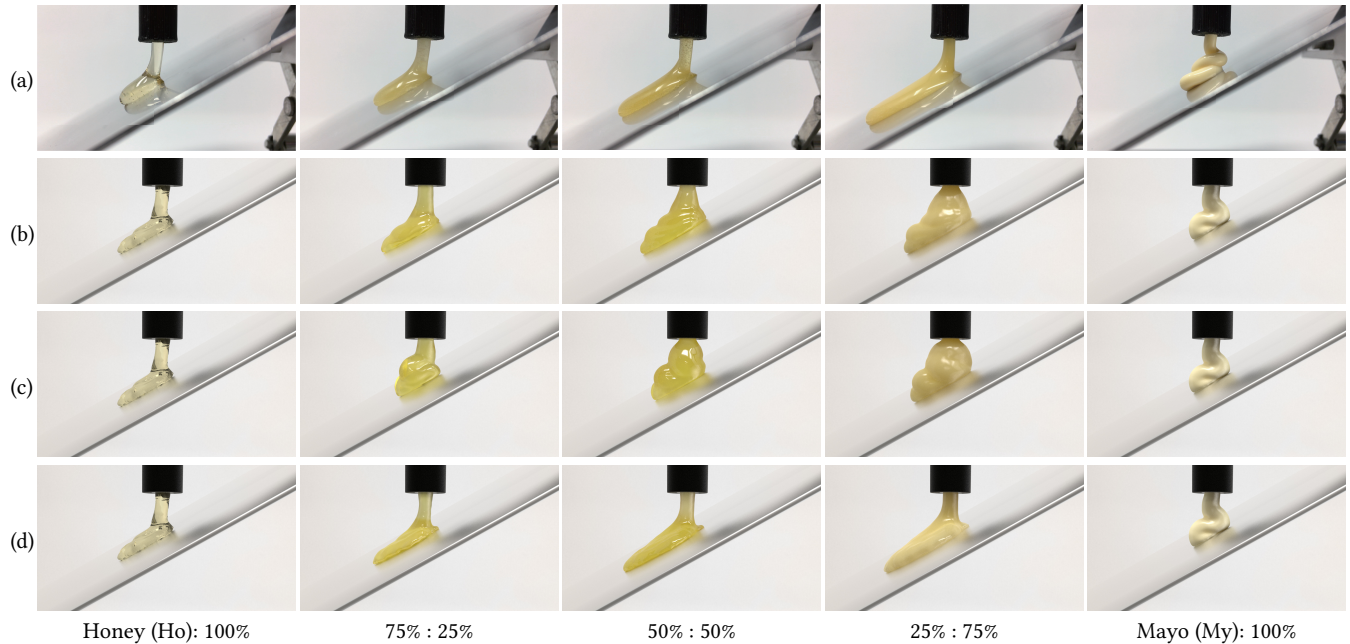


Fig. 1. Blending honey and mayo. (a) A captured footage of the mixtures with various mixing ratios. The material appears ‘stagnant’ when it is a pure mayo or a pure honey, but their mixtures flow much more smoothly. (b) With an MPM simulation using the linearly blended material parameters, the flow all looks stagnant irrespective of the mixing ratio. (c) The flow still looks stagnant when we initialize the material points with either the property of pure mayo or pure honey, with their volume fraction set according to the mixing ratio. (d) Our nonlinear blending model generates the mixed material property only using the material properties of the pure constituents and their mixing ratios, with which we can reproduce the smoothly flowing behaviors of the blended states.

The materials around us usually exist as *mixtures* of constituents, each constituent with possibly a different *elasto-viscoplastic* property. How can we describe the material property of such a mixture is the core question of this paper. We propose a nonlinear blending model that can capture intriguing flowing behaviors that can differ from that of the individual

\*Authors contributed equally.

Authors’ addresses: K. Nagasawa, T. Suzuki, M. Okada, Kiban 701, Kashiwa-no-ha 5-1-5, Kashiwa-shi, Chiba, 277-8561, Japan; R. Seto, A4-113, Katsura-Campus, Sakyo-ku, Kyoto University, Kyoto, 615-8510, Japan; Y. Yue, O-525, Fuchinobe 5-10-1, Chuo-ku, Sagamihara, Kanagawa, 252-5258, Japan.

Permission to make digital or hard copies of all or part of this work for personal or classroom use is granted without fee provided that copies are not made or distributed for profit or commercial advantage and that copies bear this notice and the full citation on the first page. Copyrights for components of this work owned by others than the author(s) must be honored. Abstracting with credit is permitted. To copy otherwise, or republish, to post on servers or to redistribute to lists, requires prior specific permission and/or a fee. Request permissions from permissions@acm.org.

© 2019 Copyright held by the owner/author(s). Publication rights licensed to ACM. 0730-0301/2019/7-ART95 \$15.00

<https://doi.org/10.1145/3306346.3322947>

constituents (Fig. 1). We used a laboratory device, *rheometer*, to measure the flowing properties of various fluid-like foods, and found that an *elastic Herschel-Bulkley model* has nice agreements with the measured data even for the mixtures of these foods. We then constructed a blending model such that it qualitatively agrees with the measurements and is closed in the parameter space of the elastic Herschel-Bulkley model. We provide validations through comparisons between the measured and estimated properties using our model, and comparisons between simulated examples and captured footages. We show the utility of our model for producing interesting behaviors of various mixtures.

CCS Concepts: • Computing methodologies → Physical simulation;

Additional Key Words and Phrases: Physical simulation, viscoplasticity, nonlinear blending, material point method, shear thinning fluids

## ACM Reference Format:

Kentaro Nagasawa, Takayuki Suzuki, Ryohei Seto, Masato Okada, and Yong-hao Yue. 2019. Mixing Sauces: A Viscosity Blending Model for Shear Thinning Fluids. *ACM Trans. Graph.* 38, 4, Article 95 (July 2019), 17 pages. <https://doi.org/10.1145/3306346.3322947>

## 1 INTRODUCTION

We daily observe a range of materials that exhibit physical behaviors in between purely elastic solid and pure fluid. On the pure fluid extreme, we have *Newtonian fluids*, with water, honey, and syrups being typical examples, where the material flows immediately in response to external forces, with the key factor for various intriguing behaviors being *viscosity*, a constant irrespective of the magnitude of the applied stress. On the purely elastic solid extreme, we have rubber-like materials, which behave like pure springs and can be described as *hyperelastic* materials. Various practical materials lie between these two extremes; they may exhibit both elastic and viscous responses, and/or the viscosity may vary and exhibit dependency on flow rate. Such materials are called *non-Newtonian fluids*. For example, mayonnaise (hereafter, ‘mayo’) stays static on top of a sausage, behaves elastically when interacting with a gentle force, and starts to exhibit viscous flow when a larger force is applied. It appears less viscous as the applied force becomes larger.

The incorporation of an appropriate *constitutive relation* between stress and strain and/or strain rate is the key to simulate various rich behaviors of the materials described above. The material point method (MPM) [Hu et al. 2018; Jiang et al. 2015, 2016; Sulsky et al. 1994, 1995] is a flexible simulation framework with which one can easily adopt a constitutive relation tailored for the material of interest.

The materials around us usually exist as *mixtures* of different constituents. In cooking, for example, we mix various fluid-like foods to make sauces, e.g., with the combination of ketchup and mayo, we can make aurora sauce. Each of the constituents of such a mixture can be Newtonian with rate-independent viscosity or non-Newtonian with rate-dependent (possibly nonlinear) viscoplasticity. The resulting material behavior of such a mixture is thus a blend of linear and/or nonlinear viscoplasticities. As the mixing ratio varies, the mixed material exhibits intriguing and nonintuitive behaviors. In Fig. 1 (a), we show a captured footage of mixtures of mayo and honey with various mixing ratios. The materials appear ‘stagnant’ for the two extreme cases: when the material is pure mayo (resp. pure honey), it does not flow much mainly because of the yield stress (resp. high viscosity). In contrast, the mixed material (half and half) exhibits a profoundly less viscous flow. In a simulation of such a mixture of materials, we are faced with the need of *modeling such blended behavior as the mixing ratio changes*.

How can we describe the material property of such a mixture is the core question of this paper. Previous approaches for simulating miscible or immiscible fluids have mainly focused on how to model the fluid interface [Kim 2010; Losasso et al. 2006b; Misztal et al. 2014] or the force that drives the fluids to mix with each other [Shin et al. 2010; Yang et al. 2015]. The question of our study is orthogonal to these previous directions. A possible approach towards the modeling of blended material behavior is to have an exhaustive database for all possible material mixtures. However, this approach would result in a combinatorial explosion of measurements. We thus alternatively pursue the study of a mathematical model for describing the blended material property with the property of each constituent and their mixing ratios as the input.

Perhaps, the two simplest approaches one would try first are (1) *linearly* blending all the material properties, and (2) assigning to each material point either the property of pure mayo or pure honey with the volume fraction of the points being equal to the mixing ratio. However, as shown in Figs. 1 (b) and (c), respectively, these two approaches do not capture the characteristic behavior: we do not see much flow irrespective of the mixing ratios. We also argue that this mismatch persists even if we increase the resolution of the simulation due to the built-in-assumption of continuum modeling (see Section 3.2). Hence, we constructed a *nonlinear* blending model that can capture the right behavior, as in Fig. 1 (d).

In a nutshell, we used a laboratory device, *rheometer*, to measure how fluid flows in response to applied forces. From the measurements of various fluid-like foods, we found that an *elastic Herschel-Bulkley model* [Yue et al. 2015] agrees well with the measured data even for mixtures of these foods. Hence, we propose a nonlinear blending model that is closed in the parameter space of the elastic Herschel-Bulkley model: we describe the material property of a mixture as a nonlinear function of the mixing ratio of each constituent and their material parameters. Furthermore, this nonlinear function satisfies the 5 properties of chemical blending [Rusin 1975].

In this study, we focus on the dynamics of the material blends, in particular thermostatic cases without chemical reactions; we leave the treatment for temperature dependency, chemical reactions, and optical blending as future work. Note that in rheology, there is no ground understanding of the blended properties of non-Newtonian fluids. We pursue a phenomenological approach. Because of the availability and accuracy in the measurements of the materials, we limit the scope of our target to shear thinning fluids, with detailed limitations discussed in Section 4.

We provide validations through comparisons between the measured and estimated properties using our model, and comparisons between simulated and captured examples. We show the utility of our model for producing interesting behaviors of various mixtures.

## 2 RELATED WORK

A tremendous number of techniques have been developed to simulate materials ranging from pure fluids to purely elastic solids. We briefly review the material modeling as well as the integrators.

### 2.1 Material modeling of fluids and solids

Extending the Navier-Stokes formulation for the pure (viscous) *fluid* regime [Foster and Metaxas 1996], Goktekin et al. [2004] incorporated viscoelastic fluids. Zhu and Bridson [2005] have shown that a collection of discrete grains can be modeled as a fluid, and Narain et al. [2010] later reformulated the granular fluid model as a linear complementarity problem.

Building on the Lagrangian finite element method (FEM) framework for *solids*, Terzopoulos and Fleischer [1988] introduced the viscoplastic model. Later, Irving et al. [2004] introduced invertible finite elements for simulating elastic solids and plasticity.

While these two branches of research may seem independent (one emerges from the pure fluid regime and the other emerges from the pure solid regime), it can be shown that the fluid-based formulation

can be regarded as a special case of the solid-based formulation (as discussed in Section 5.2).

Since the recent introduction of the material point method (MPM) [Sulsky et al. 1994, 1995] to snow simulation [Stomakhin et al. 2013], a variety of materials have been simulated thanks to its flexibility and easiness of incorporating various constitutive models. Stomakhin et al. [2014] extended the MPM to incorporate phase transitions, and Ram et al. [2015] introduced the Oldroyd-B plasticity model [Oldroyd and Wilson 1950] to simulate sponge, cream, and toothpaste. Yue et al. [2015] combined a hyperelastic model together with the Herschel-Bulkley model [Herschel and Bulkley 1926], which we call *elastic Herschel-Bulkley* model in this paper, to simulate various shear dependent flows, including creams with the shear-thinning effect, as well as oobleck with the shear-thickening effect. Shear-thinning (resp. shear-thickening) materials are easier (resp. harder) to flow at a larger shear rate. Concurrently, Zhu et al. [2015] introduced the Carreau-Yasuda model [Carreau 1972; Yasuda 1979] to a Lagrangian FEM technique to simulate co-dimensional non-Newtonian effects. Wretborn et al. [2017] extended the MPM for the simulation of cracks, and Bacchini et al. [2017] for magnetized fluids. Dunatunga and Kamrin [2015], Klar et al. [2016], and Daviet and Bertails-Descoubes [2016] introduced the Drucker-Prager yield condition [Drucker and Prager 1952] for the continuum simulation of granular materials. Combining the continuum approach with a penalty-based discrete element approach [Cundall and Strack 1979], Yue et al. [2018] proposed a hybrid technique for simulating granular materials with accurate handling of contacts between the grains and boundaries or obstacles, as well as rolling, bouncing and, ballistic motions near free surfaces.

Among different material models discussed above, we found that the elastic Herschel-Bulkley model [Yue et al. 2015] is more suitable for fluid-like foods, which are of interest to us.

## 2.2 Integrators for fluids and solids

**2.2.1 Eulerian/hybrid Eulerian-Lagrangian approaches.** Extending the Navier-Stokes solver [Foster and Metaxas 1996] with a semi-Lagrangian approach [Stam 1999] and particle-based level set approaches, Foster and Fedkiw [2001] and Enright et al. [2002] improved on the robustness of the simulation and the details of the results. These techniques were further extended to handle interactions between multiple fluids [Carlson et al. 2002; Hong and Kim 2005; Losasso et al. 2006a,b] and interactions between solids and fluids [Carlson et al. 2004; Robinson-Mosher et al. 2008]. While the semi-Lagrangian-based approach suffered from volume loss and excessive numerical diffusion, recent fluid simulation techniques build on a hybrid Eulerian grid and Lagrangian particle approach called FLIP [Zhu and Bridson 2005] to overcome such issues. The FLIP approach was further extend using a hierarchical approach [Ando et al. 2013] and narrow band approach [Ferstl et al. 2016] for better performance. For simulating thin film features, Brochu et al. [2010] combined an Eulerian liquid simulation framework with a Voronoi diagram. For robust and efficient handling of irregular boundary geometries, Batty et al. [2007] proposed a variational framework for the pressure projection operator, which was later extended to a unified pressure and viscosity solver [Larionov et al. 2017].

**2.2.2 SPH based approaches.** Smooth particle hydrodynamics (SPH) [Müller et al. 2003] is a purely particle-based fluid simulator. Accurately and efficiently enforcing the divergence-free condition is key to the reproduction of intriguing vortices; techniques allowing for a little compressibility [Becker and Teschner 2007] and for fully enforcing incompressibility [Bender and Koschier 2015; Ihmsen et al. 2014; Solenthaler and Pajarola 2009] have been proposed in this regard. Peer et al. [2015] proposed to implicitly handle the viscosity for efficiency in highly stiff situations.

The SPH framework has been extended to handle various materials, including deformable solids [Becker et al. 2009], viscoelastic fluids [Chang et al. 2009; Clavet et al. 2005], viscoplasticity [Gerszewski et al. 2009; Jones et al. 2014], non-Newtonian fluids [Paiva et al. 2006, 2009], foams [Cleary et al. 2007], and porous flows [Lenaerts et al. 2008]. It has also been extended to fluid-solid interactions [Müller et al. 2004; Solenthaler et al. 2007], fluid-fluid interactions [Mao and Yang 2006; Müller et al. 2005], multi-phase, miscible fluids [Ren et al. 2014; Yan et al. 2016; Yang et al. 2015], and a generalization to a pair-wise force model for incorporating various interactions at the interface [Yang et al. 2017].

**2.2.3 Lagrangian FEM based approaches.** Building on the finite element method (FEM) for simulating elastic solids, Bargteil et al. [2007] incorporated remeshing for simulating solids with large plastic deformations. Wojtan et al. [2008] proposed a hybrid method that combines Lagrangian surface meshes with an adaptive body-centered cubic (BCC) lattice for simulating viscoelastic materials with thin features. This approach was extended to handle topological changes [Wojtan et al. 2009], plasticity with a high-quality material space mesh undergoing plastic flow [Wicke et al. 2010], liquid simulations and solid-liquid interactions [Clausen et al. 2013], and multi-phase immiscible fluids [Misztal et al. 2014]. To accurately incorporate co-dimensional elements, Bergou et al. [2010] proposed a fluid-as-thread paradigm for the simulation of viscous threads, and this was later extended by Batty et al. [2012] to simulate viscous sheets.

**2.2.4 Position/constraint-based approaches.** Barreiro et al. [2017] extended the position-based dynamics framework [Macklin and Müller 2013; Müller et al. 2007] to handle viscoelastic materials with the incorporation of constitutive models, and He et al. [2018] incorporated a peridynamics- and constraint-based approach (in essence an integral form for incorporating constitutive models) for simulating elastic, viscoelastic, and Drucker-Prager materials.

**2.2.5 MPM based approaches.** The material point method (MPM) [Stomakhin et al. 2013; Sulsky et al. 1994, 1995] is an extension of the FLIP approach to solid mechanics by incorporating particle-based treatment of constitutive models, including history dependency. Besides the MPM's ease in handling a variety of constitutive models, researchers have worked on improving its built-in transfer projection operator to better conserve energy and vorticity [Fu et al. 2017; Jiang et al. 2015], improve its performance and ease of implementation [Hu et al. 2018], improve the particle distributions [Yue et al. 2015], incorporate velocity discontinuities [Moutsanidis et al. 2019], parallelize the MPM using GPUs [Gao et al. 2018], improve stability by generalizing the particle-side basis functions [Bardenhagen and

Kober 2004; Sadeghirad et al. 2011; Zhu et al. 2017], incorporate spatially adaptive elements [Gao et al. 2017], perform asynchronous time stepping [Fang et al. 2018], incorporate co-dimensional elements for elastoplasticity in cloth, knit, and hair [Jiang et al. 2017], and robustly and efficiently handle fluid-solid interactions [Yan et al. 2018].

We chose the MPM for testing our nonlinear blending model, because of its easiness of incorporating the constitutive model that may result in a large deformation without the need for remeshing, and because the MPM provides more accurate and more stable results than a purely particle-based method [Yan et al. 2018].

### 2.3 Simulating miscible fluids

To simulate miscible and immiscible fluids, Park et al. [2008] introduced the Cahn-Hilliard Equation [Cahn and Hilliard 1958] and implemented it with a Lattice Boltzmann Method (LBM). The Cahn-Hilliard Equation is a partial differential equation describing the phase mixing and separation process, with which one can model intriguing fluid mixing automatically through a chemical potential. This approach was incorporated into a Navier-Stokes-Cahn-Hilliard system, demonstrated with implementation on both SPH and position-based frameworks, by Yang et al. [2015] with a non-convex chemical potential to simulate unintuitive phase separation and dissolving processes. Yang et al. [2017] further incorporated a phase-field method into the SPH framework to account for multi-material simulation with phase transitions and soluble and insoluble interactions. To simulate a mixture of water and sand, a two-grid MPM-based approach [Pradhana 2017; Pradhana et al. 2017] was proposed to account for momentum changes between the two materials. This approach was then extended to simulate fluid sediment mixture in a particle-laden flow [Gao et al. 2018].

These methods do not account for the unintuitive viscosity blending of multiple materials, which is the main focus of this paper.

### 2.4 Empirical viscosity blending

There are various empirical viscosity-blending models known for Newtonian fluids [Zhmud 2014], typically those well studied in the oil industry (e.g., lubricants and fuels), to calculate the mixed viscosity  $\eta$  of two constituents with viscosity  $\eta_A$  and  $\eta_B$  blended at the mixing ratio  $\alpha$  (in the sense that  $A$  and  $B$  have the volume fractions  $\alpha$  and  $1 - \alpha$ , respectively). Popular models (as we discuss in detail in Section 4.4) include the Arrhenius equation [Arrhenius 1887], Bingham equation [Bingham and Brown 1932; Jones and Bingham 1905], Kendall and Monroe model [Kendall and Monroe 1917], and Refutas method [American Society for Testing and Materials 2016]. Each of these models is a particular form of the general mixing function (18). In essence, they all produce viscosities that are sub-linear (i.e.,  $\eta < \alpha\eta_A + (1 - \alpha)\eta_B$  for  $0 < \alpha < 1$  and  $\eta_A \neq \eta_B$ ). When blending two materials with the same viscosity (i.e.,  $\eta_A = \eta_B$ ), the viscosity of the mixed material becomes  $\eta = \eta_A = \eta_B$ , irrespective of the mixing ratios. However, this is not the case for a mixture of non-Newtonian fluids, as we discuss in detail in Section 3.

There are also models specialized for a particular pair of constituents (binary blending). One of the simplest models in this class is perhaps the Lederer and Roegiers' model [Lederer 1931; Roegiers

and Roegiers 1946], which belongs to the form of (27). As we show later, the constants in such models cannot be chosen independently from the pair of materials, meaning that we need to measure such constants for every pair of materials that are of interest. Even worse, a blend of *blended materials* has to be treated as a new material, making it ineffective for simulation of several materials blended with a dynamically changing mixing ratio. Likewise, even more involved binary blending models with higher order terms that appear in industrial blending processes, including pharmaceuticals and cosmetics, are ruled out from our purpose, which is to deliver an easy-to-use blending model for practitioners without sophisticated measurement equipment (i.e., animators) to produce dynamical blending animations with qualitative agreement with the observations of a certain class of materials.

## 3 MEASUREMENTS AND MODEL FITTING

We use a laboratory device, *rheometer* (Anton-Paar Modular Compact Rheometer MCR 92, Fig. 2(a)), to measure the flow curves of various materials, a relationship between the stress  $\sigma$  and strain rate  $\dot{\epsilon}$ . A rotational or shear rheometer works by sandwiching a specimen with a static mounting plate (a flat surface) and a geometry that rotates at a constant controlled speed (Figs. 2(b) and (c)) and measuring the torque needed to maintain the rotation. Both boundary conditions at the flat surface and the geometry are assumed to be non-slip.

A typical choice of the geometry shape is a symmetric cone because one can apply the same strain rate anywhere inside the specimen in principle. That is, in a cross section around the rotation axis (Fig. 2(c)), the motion speed  $s$  of the specimen varies linearly as  $s = L\omega$ , where  $\omega$  is the angular speed of the rotation, and  $L$  is the arm length, related to the height  $H$  linearly as  $H = L \cdot \tan \theta$ , where  $\theta$  is the angle of the cone; hence,  $s = H\omega/\tan \theta$ . Because the specimen is so thin, usually with  $\theta = 0.5^\circ$  or  $1.0^\circ$ , the vertical speed can be assumed to vary linearly according to the height  $H$ ; thus, we have a constant shear rate  $\dot{\epsilon} = s/H = \omega/\tan \theta$ .

We also use a parallel plate, a common alternative to the cone geometry when the specimen contains inclusions, like pepper in a hot chili sauce. We tested measurements using a cone geometry and a parallel plate for specimens with and without inclusions, and found that the results were more or less the same for moderate strain rates and that the parallel plate provided more stable measurements for low and high strain rates for specimens with inclusions.

By definition, viscosity  $\eta$  is the ratio between the applied stress  $\sigma$  and the strain rate  $\dot{\epsilon}$ , i.e.,  $\eta = \sigma/\dot{\epsilon}$ , and can be directly deduced from the measurements by using a rheometer. In a Newtonian fluid, the viscosity is a constant irrespective of the strain rate; thus, the flow curve corresponding to a Newtonian fluid is expected to be a straight line passing through the origin in a linear scale plot, where the slope identifies the viscosity. With any curve apart from this family of straight lines, we deduce that the measured specimen is a non-Newtonian fluid (Fig. 2(d)), where the *effective viscosity* (defined as the slope of the line connecting the origin and the corresponding point in the flow curve) is a (non-constant) function of the strain rate.

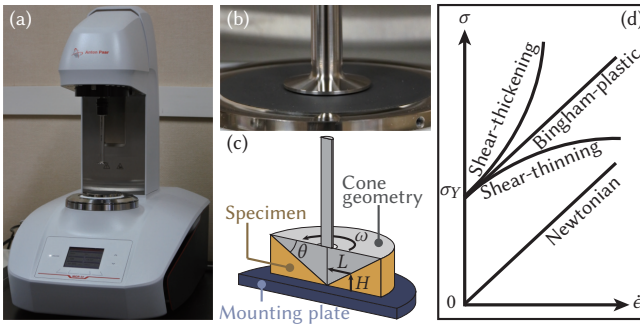


Fig. 2. (a) The rheometer, Anton-Paar Modular Compact Rheometer MCR 92, used for our tests. (b) A close up of the mounting plate and the cone geometry, and (c) an illustrative cross section view of them. (d) Various flow curves and their corresponding physical properties.

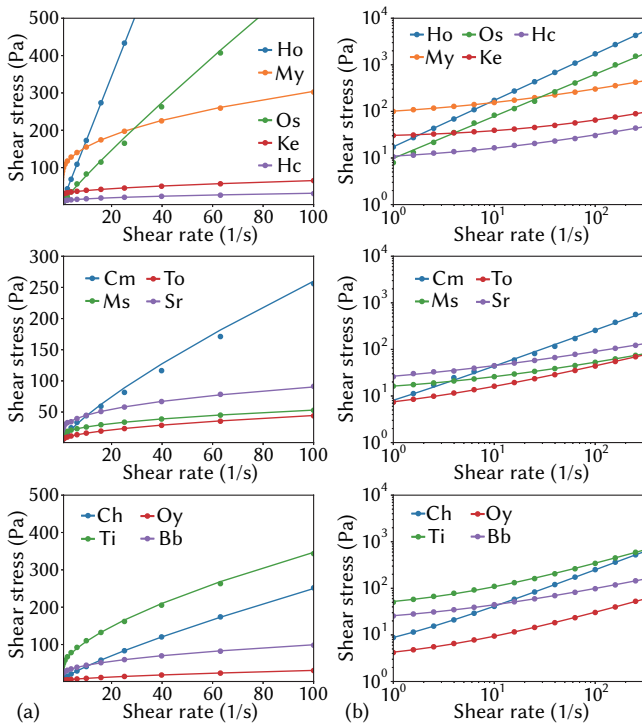


Fig. 3. Flow curves in (a) a linear scale and (b) a logarithmic scale, with the solid lines denoting curves fitted to the Herschel-Bulkley model (1). Please see Table 1 for the meanings of the abbreviations of the material labels.

### 3.1 Herschel-Bulkley viscoplasticity

Figs. 3 (a) and (b) show the measured data (the dots in the figures), plotted in (a) linear and (b) logarithmic scales. The range of the shear rate in our measurements and analyses was consistently chosen to be  $1\text{s}^{-1}$  to  $200\text{s}^{-1}$ . From Fig. 3 (a), it is apparent that many materials possess highly nonlinear behavior in viscosity, and from Fig. 3 (b), we can see that the relation between the stress and strain rate can be almost fit by a straight line in the logarithmic scale. This implies that

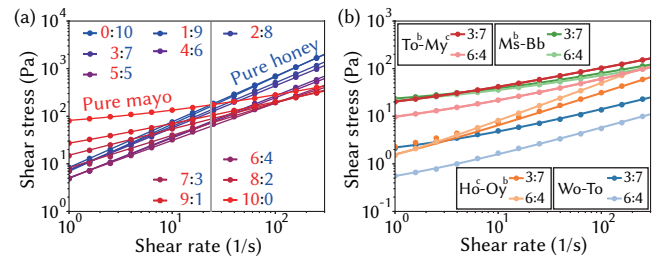


Fig. 4. (a) Flow curves of the honey ( $\text{Ho}^b$ ) - mayo ( $\text{My}^b$ ) mixtures for various mixing ratios. (b) Flow curves of various mixtures. The solid lines show curves fitted to the Herschel-Bulkley model (1).

Table 1. Material parameters for various sauces and syrups. Superscripts ‘b’ and ‘c’ indicate alternate measurements of the same material, possibly with a slightly different condition. The measurements were done in an air-conditioned room at around  $19^\circ\text{C}$ , with the exceptions of ‘ $\text{Ho}^b$ ’, ‘ $\text{My}^b$ ’, ‘ $\text{My}^c$ ’, and ‘ $\text{To}^b$ ’, which were measured in an air-conditioned room at around  $25^\circ\text{C}$ . The viscosity of honey is known to have strong dependency on temperature.

Specimen, Brand	temperature	$h$	$\eta [\text{Pa} \cdot \text{s}^h]$	$\sigma_Y [\text{Pa}]$	Geometry
Honey (Ho), SEVEN & i PREMIUM	$19.27^\circ\text{C}$	0.997	17.4	$4.06 \times 10^{-7}$	Cone
Honey ( $\text{Ho}^b$ ), SEVEN & i PREMIUM	$26.2^\circ\text{C}$	0.995	6.88	$8.42 \times 10^{-2}$	Cone
Honey ( $\text{Ho}^c$ ), SEVEN & i PREMIUM	$19.56^\circ\text{C}$	0.971	18.1	$1.0 \times 10^{-6}$	Parallel
Mayo (My), Kewpie	$19.0^\circ\text{C}$	0.442	30.5	70.8	Cone
Mayo ( $\text{My}^b$ ), Kewpie	$25.4^\circ\text{C}$	0.450	28.9	53.0	Cone
Mayo ( $\text{My}^c$ ), Kewpie	$23.73^\circ\text{C}$	0.421	24.0	41.3	Parallel
Oligosaccharide syrup (Os), SEVEN & i PREMIUM	$18.39^\circ\text{C}$	0.903	9.82	$4.71 \times 10^{-7}$	Cone
Ketchup (Ke), KAGOME	$19.71^\circ\text{C}$	0.524	3.4	27.2	Parallel
Hot chilli sauce (Hc), GOLDEN MOUNTAIN	$19.22^\circ\text{C}$	0.456	2.85	8.11	Parallel
Sweetened condensed milk (Cm), Morinaga Milk	$19.02^\circ\text{C}$	0.782	7.08	1.03	Parallel
Mustard (Ms), S&B	$19.18^\circ\text{C}$	0.447	5.4	10.9	Parallel
Mustard ( $\text{Ms}^b$ ), S&B	$20.03^\circ\text{C}$	0.461	5.08	12.5	Parallel
Japanese pork cutlet sauce (To), Bull-Dog	$19.02^\circ\text{C}$	0.518	3.75	3.74	Parallel
Japanese pork cutlet sauce ( $\text{To}^b$ ), Bull-Dog	$25.65^\circ\text{C}$	0.510	3.67	3.63	Parallel
Sriracha hot chilli sauce (Sr), Flying Goose Brand	$18.3^\circ\text{C}$	0.396	12.3	14.3	Parallel
Chocolate syrup (Ch), Morinaga	$18.63^\circ\text{C}$	0.809	5.96	2.84	Cone
Sweat bean sauce (Ti), LEE KUM KEE	$19.27^\circ\text{C}$	0.629	17.2	35.0	Parallel
Oyster sauce (Oy), SEVEN & i PREMIUM	$18.8^\circ\text{C}$	0.62	1.61	2.65	Parallel
Oyster sauce ( $\text{Oy}^b$ ), SEVEN & i PREMIUM	$18.29^\circ\text{C}$	0.618	1.63	2.61	Parallel
BBQ sauce (Bb), McDonald's Japan, BBQ Sauce	$18.59^\circ\text{C}$	0.48	9.28	16.5	Parallel
Worcestershire sauce (Wo), Bull-Dog	$19.02^\circ\text{C}$	0.928	0.012	0.016	Parallel

the flow curve can be described using the *Herschel-Bulkley model*:

$$\sigma = \sigma_Y + \eta \dot{\epsilon}^h, \quad (1)$$

where  $\sigma_Y$  is the yield stress,  $h$  is the Herschel-Bulkley power, and  $\eta$  is the consistency parameter (when  $h = 1$ ,  $\eta$  becomes viscosity). The solid curves in Fig. 3 are the fitted results and show excellent agreements with the measurements. We employed the fitting by solving the following minimization problem per material:

$$(\sigma_Y, \eta, h) = \operatorname{argmin}_{\sigma'_Y, \eta', h'} \sum_{i=1}^N \left\| \frac{\sigma'_Y + \eta' \dot{\epsilon}_i^{h'} - \tilde{\sigma}_i}{\tilde{\sigma}_i} \right\|^2, \quad (2)$$

where  $N$  is the number of different strain rate samples in the measurements, and  $\dot{\epsilon}_i$  and  $\tilde{\sigma}_i$  are the strain rate and stress of the  $i$ -th sample. Note that the error is measured in the *relative* sense, to account for the fact that both the strain rate and stress of our interest range in several orders of magnitude; we want to have a good fit for both high and low strain rate regimes. We show the material parameters obtained from our measurements and fitting in Table 1.

### 3.2 Viscoplasticity of mixtures

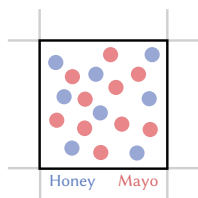
We also measured the stress/strain-rate relation for mixed materials. Fig. 4(a) shows the results of mixtures of honey and mayo with various mixing ratios and those fitted to the Herschel-Bulkley model, and Fig. 4(b) shows several measurements of other mixtures and the corresponding fittings. Before these measurements, we prepared the substances by stewing each with a fixed amount of time, for not only the mixtures but also the (pure) constituents. We also paid attention to the consistency in the temperature and geometry, and made alternate measurements of the same material for the use in the mixture as needed (materials with superscripts ‘b’ or ‘c’) in Table 1. From the fitting, we can see that the viscosity behavior of the mixtures are all nicely fitted by the Herschel-Bulkley model as well. Hence, we are encouraged to consider models of mixtures that are *closed* in the parameter space of the Herschel-Bulkley model, which is the intention with our model design.

A noticeable property from Fig. 4(a) is that the stresses of the mixtures of various mixing ratios are smaller than those of the constituents at the strain rate of  $22\text{s}^{-1}$  (the gray line in Fig. 4(a)), where the stresses of the constituents coincide. In other words, the *effective viscosities* of the two constituents coincide at the point, but those of their mixtures are lower. The reduction in the viscosity of this example is almost an order of magnitude and cannot be ignored (as we demonstrated in Fig. 1). We also conducted the measurements several times, and the flow curves were more or less the same.

Conventional blending models [American Society for Testing and Materials 2016; Arrhenius 1887; Bingham and Brown 1932; Jones and Bingham 1905; Kendall and Monroe 1917] have the form (18):  $F(\eta) = \alpha F(\eta_A) + (1-\alpha)F(\eta_B)$ , where  $\alpha$  is the mixing ratio,  $\eta_A$  and  $\eta_B$  are the viscosities of the two constituents, and  $F$  is an invertible function that depends on the model. These models all fail to capture this characteristic behavior, because when  $\eta_A = \eta_B$ , their predictions all provide  $\eta = \eta_A = \eta_B$ , irrespective of the choice of  $\alpha$  and  $F$ .

In addition, having multiple material points with different material parameters in a single cell would simply result in a *linear* blending of the effective viscosity. This can be seen from the fact that multiple material points at the same location (or we can alternatively assume that the cell is sufficiently small) would have the same strain rate  $\dot{\epsilon}$ , and that the resulting stress  $\sigma$  would be given by  $\sigma = \frac{\sum_i V_i \eta_i \dot{\epsilon}}{\sum_k V_k} = \dot{\epsilon} \sum_i \alpha_i \eta_i$ , where  $V_i$  is the volume of the  $i$ -th particle, and  $\alpha_i = \frac{V_i}{\sum_k V_k}$  is its volume fraction. Because all particles at the same location have the same change in volume  $J$  (the determinant of the deformation gradient), it does not matter whether the deformed or undeformed volumes are used in this argument, as only the ratio between volumes matters. Hence, the effective viscosity  $\eta = \sigma/\dot{\epsilon} = \sum_i \alpha_i \eta_i$  is a linear blending of the viscosities of the constituents.

Finally, note that simply refining the continuum simulation does not mean the reproduced physics will asymptotically approach the actual physics occurring at the microscopic level. This is because of the underlying continuum assumption behind the constitutive modeling: it accounts for the macroscopic *homogenized* behavior



of a *collection* of microscopic constituent particles (molecules, colloidal particles, polymers, etc.), and includes their interactions and collective behaviors.

Therefore, we are faced with the fact that the characteristic behavior we observed from the plots and captured footage can be reproduced neither by using a blending model that only accounts for the effective viscosity and mixing ratio, nor by hoping that the MPM framework would generate the desired result by simply mixing different particles. This point implies the necessity for a blending model that extends to non-Newtonian fluids.

## 4 BLENDING MODEL

For simplicity, we assume that the blending process is both mass and volume conserving. Mathematically, we characterize a *substance*  $\mathbb{S}$  by its mass  $m$  and a set of *material* parameters  $\mathbf{M}$ , i.e.,  $\mathbb{S} := (m, \mathbf{M})$ . A blending model defines how a substance  $\mathbb{S}_C$  can be represented by its constituents, for instance,  $\mathbb{S}_A$  and  $\mathbb{S}_B$ , or equivalently, how we can define the blending operator  $\otimes$  such that  $\mathbb{S}_C = \mathbb{S}_A \otimes \mathbb{S}_B$ .

We ask that a blending model satisfies a set of consistency properties. Rusin [1975] introduced 5 such properties for chemical blending and introduced the mass conservation as an option (he called it *additivity*). He also showed that when we have the 5 properties, together with additivity and the uniqueness in the decomposition, the blending operator  $\otimes$  admits a general functional form (18). Our design of the nonlinear viscosity blending model is thus to make a particular choice of the functional form.

### 4.1 Laws of blending

We consider the following six laws of blending (i.e., the 5 properties of Rusin [1975] together with the mass conservation).

**4.1.1 Commutative law.** The commutative law states that the left and right sides of the operator  $\otimes$  are interchangeable, or equivalently, that blending  $\mathbb{S}_A$  into  $\mathbb{S}_B$  and blending  $\mathbb{S}_B$  into  $\mathbb{S}_A$  should result in the same substance:

$$(m_A, \mathbf{M}_A) \otimes (m_B, \mathbf{M}_B) = (m_B, \mathbf{M}_B) \otimes (m_A, \mathbf{M}_A). \quad (3)$$

**4.1.2 Distributive law.** The distributive law states that multiplying the masses of the constituents with the same factor will result in a substance with the mass scaled to the same factor but without changing the material property, i.e., if the following equation holds for  $k = 1$ , then it holds for any positive  $k > 0$ :

$$(km_A, \mathbf{M}_A) \otimes (km_B, \mathbf{M}_B) = (km_C, \mathbf{M}_C). \quad (4)$$

**4.1.3 Zero law.** The zero law states that mixing a substance of positive mass ( $m_A > 0$ ) with any material of *zero* mass has no effect:

$$(m_A, \mathbf{M}_A) \otimes (0, \mathbf{M}_B) = (m_A, \mathbf{M}_A). \quad (5)$$

**4.1.4 Associative law.** The associative law states that an application of a sequence of blending operations would result in the same substance, irrespective of the (associative) order of the operations:

$$\begin{aligned} & ((m_A, \mathbf{M}_A) \otimes (m_B, \mathbf{M}_B)) \otimes (m_C, \mathbf{M}_C) \\ &= (m_A, \mathbf{M}_A) \otimes ((m_B, \mathbf{M}_B) \otimes (m_C, \mathbf{M}_C)). \end{aligned} \quad (6)$$

Together with the commutative law, the associative law states that the result of the mixing does not depend on the path (or order) of

blending. This is a natural characteristic we would ask physically, especially in the absence of chemical reactions.

**4.1.5 Identity law.** The identity law states that mixing two substances with the same material would result in a substance with identical material and the summed mass:

$$(m_{A1}, \mathbf{M}_A) \otimes (m_{A2}, \mathbf{M}_A) = (m_{A1} + m_{A2}, \mathbf{M}_A). \quad (7)$$

**4.1.6 Mass conservation law.** In the absence of nuclear reactions, it is natural to ask

$$(m_A, \mathbf{M}_A) \otimes (m_B, \mathbf{M}_B) = (m_A + m_B, \mathbf{M}_C). \quad (8)$$

## 4.2 General mixing model

Combining the mass conservation law (8) with the distributive law (4), setting  $k = \frac{1}{m_A + m_B}$ , and letting  $\alpha = \frac{m_A}{m_A + m_B}$ , we have

$$(\alpha, \mathbf{M}_A) \otimes (1 - \alpha, \mathbf{M}_B) = (1, \mathbf{M}_C), \quad (9)$$

where  $\alpha$  represents the *mixing ratio*. (9) implies that the mixed material  $\mathbf{M}_C$  can be represented as a map  $G$  of  $\alpha$ ,  $\mathbf{M}_A$ , and  $\mathbf{M}_B$ :

$$\mathbf{M}_C = G(\alpha, \mathbf{M}_A, \mathbf{M}_B). \quad (10)$$

## 4.3 Laws in the map $G$

As expected, the laws of blending can be re-casted as a set of laws on  $G$ . The commutative law can be re-casted as

$$G(\alpha, \mathbf{M}_A, \mathbf{M}_B) = G(1 - \alpha, \mathbf{M}_B, \mathbf{M}_A). \quad (11)$$

The distributive law is already incorporated to the form of  $G$  through the use of the mixing ratio (rather than mass) as the first argument. The zero law can be re-casted as

$$G(0, \mathbf{M}_A, \mathbf{M}_B) = \mathbf{M}_B, \quad (12)$$

$$G(1, \mathbf{M}_A, \mathbf{M}_B) = \mathbf{M}_A. \quad (13)$$

The associative law can be re-casted as

$$\begin{aligned} & G\left(\frac{m_A + m_B}{m_A + m_B + m_C}, G\left(\frac{m_A}{m_A + m_B}, \mathbf{M}_A, \mathbf{M}_B\right), \mathbf{M}_C\right) \\ &= G\left(\frac{m_A}{m_A + m_B + m_C}, \mathbf{M}_A, G\left(\frac{m_B}{m_B + m_C}, \mathbf{M}_B, \mathbf{M}_C\right)\right). \end{aligned} \quad (14)$$

The identity law can be re-casted as

$$G(\alpha, \mathbf{M}, \mathbf{M}) = \mathbf{M}. \quad (15)$$

**4.3.1 Family of  $G$ .** The family  $\mathcal{G}$  of this map  $G$  is a general function space of blending that includes the standard linear blending model  $L \in \mathcal{G}$ :

$$\mathbf{M}_C := L(\alpha, \mathbf{M}_A, \mathbf{M}_B) = \alpha \mathbf{M}_A + (1 - \alpha) \mathbf{M}_B, \quad (16)$$

as well as the multiplicative blending model  $X \in \mathcal{G}$ :

$$\mathbf{M}_C := X(\alpha, \mathbf{M}_A, \mathbf{M}_B) = \mathbf{M}_A^\alpha \odot \mathbf{M}_B^{(1-\alpha)}, \quad (17)$$

where  $\odot$  indicates the component-wise multiplication, and the power is defined in a component-wise manner as well. Rusin [1975] pointed out a general class of the family  $\mathcal{G}$  in the form:

$$\mathbf{M}_C = G(\alpha, \mathbf{M}_A, \mathbf{M}_B) := F^{-1}(\alpha F(\mathbf{M}_A) + (1 - \alpha) F(\mathbf{M}_B)), \quad (18)$$

where  $F$  is an arbitrary invertible map that preserves the dimensionality of the material parameters. In fact, setting  $F$  to the identity map, we recover the linear blending model, and to the component-wise

logarithmic map, we recover the multiplicative blending model. (18) can be viewed as a linear blending in the space *warped* by the map  $F$ :

$$F(\mathbf{M}_C) = L(\alpha, F(\mathbf{M}_A), F(\mathbf{M}_B)) = \alpha F(\mathbf{M}_A) + (1 - \alpha) F(\mathbf{M}_B). \quad (19)$$

Before we describe our design, we review previous empirical viscosity blending models to reveal one more important insight.

## 4.4 Empirical viscosity blending in Newtonian fluids

Many empirical models for viscosity blending of Newtonian fluids have the general form (18). The Arrhenius equation [1887] is a multiplicative blending model with the choice of  $F(x) = \ln(x)$ :

$$\ln \eta = \alpha \ln \eta_A + (1 - \alpha) \ln \eta_B. \quad (20)$$

With the reciprocal function  $F(x) = 1/x$ , we recover the Bingham equation [Bingham and Brown 1932; Jones and Bingham 1905]:

$$\eta^{-1} = \alpha \eta_A^{-1} + (1 - \alpha) \eta_B^{-1}, \quad (21)$$

with the choice of the one-thirds power,  $F(x) = x^{1/3}$ , we recover the Kendall and Monroe model [1917]:

$$\eta^{1/3} = \alpha \eta_A^{1/3} + (1 - \alpha) \eta_B^{1/3}, \quad (22)$$

and with the choice of  $F(x) = 14.534 \ln(\ln(x + 0.8)) + 10.975$ , we recover the Refutas method [American Society for Testing and Materials 2016]:

$$\eta = \exp\left(\exp\left(\frac{\alpha \tilde{\eta}_A + (1 - \alpha) \tilde{\eta}_B - 10.975}{14.534}\right)\right) - 0.8, \quad (23)$$

where  $\tilde{\eta}_* = 14.534 \ln(\ln(\eta_* + 0.8)) + 10.975$  for  $* = A, B$ . Note that the Refutas method can be well approximated by  $\eta^{-0.384} = \alpha \eta_A^{-0.384} + (1 - \alpha) \eta_B^{-0.384}$  with a relative error of less than 0.7%.

With the models (20), (21), (22), and (23) listed above, the calculated viscosity of an intermediate mixing ratio  $0 < \alpha < 1$  satisfies  $\eta = \eta_A = \eta_B$  for the case  $\eta_A = \eta_B$ , irrespective of the choice of  $\alpha$ , as discussed in Section 3.2, and for  $\eta_A \neq \eta_B$ , a sublinear property  $\eta < \alpha \eta_A + (1 - \alpha) \eta_B$  (i.e., smaller than the linear estimate), as seen from the inset.

Outside the form (18), we have, for example, the Lederer and Roegiers' model [Lederer 1931; Roegiers and Roegiers 1946]:

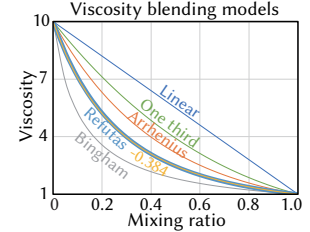
$$\ln \eta = \frac{x_A}{x_A + \beta x_B} \ln \eta_A + \frac{\beta x_B}{x_A + \beta x_B} \ln \eta_B, \quad (24)$$

where  $x_A$  and  $x_B$  are the volume fractions of materials A and B, respectively, and  $\beta$  is an empirical parameter. Because the mixing ratio  $\alpha$  is related to  $x_A$  and  $x_B$  via

$$\alpha = \frac{x_A}{x_A + x_B} = \frac{1}{1 + x_B/x_A}, \quad (25)$$

we can rewrite (24) as

$$\ln \eta = \frac{\alpha}{\alpha + \beta(1 - \alpha)} \ln \eta_A + \left(1 - \frac{\alpha}{\alpha + \beta(1 - \alpha)}\right) \ln \eta_B. \quad (26)$$



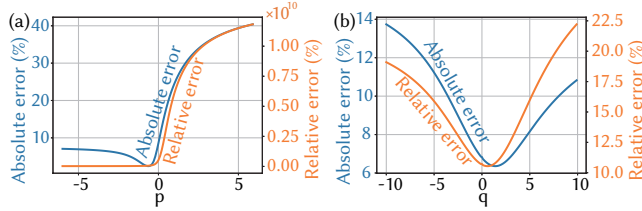


Fig. 5. (a) The relative and absolute errors in predicting  $\sigma_{Y,M}$  vs. the parameter  $p$ . The absolute error is divided by the maximum value of the measured yield stress of the mixtures for a normalization. (b) The relative and absolute errors in predicting  $h$  vs. the parameter  $q$ . Again, the absolute error is divided by the maximum value of the  $h$  parameters from the measurements for a normalization.

Writing  $\phi(\alpha; \beta) = \frac{\alpha}{\alpha + \beta(1-\alpha)}$ , we see that the Lederer and Roegiers' model belongs to the following class ( $\phi \in \Phi$ ):

$$F(\eta) = \Phi(\alpha; \beta)F(\eta_A) + (1 - \Phi(\alpha; \beta))F(\eta_B), \quad (27)$$

which is a generalized version of (18).

Now the question is whether  $\beta$  in (27) can be chosen *independently* from the pair of materials  $A$  and  $B$ . If not, this means the model needs to be tuned per combination, which could be hard for design. We see in Appendix A that the following theorem is true.

**THEOREM 4.1.** *If we assume that  $\beta$  in  $\Phi(\alpha; \beta)$  does not depend on the constituents, i.e., if we can write  $\tilde{\Phi}(\alpha) = \Phi(\alpha; \beta)$  in (27), then  $\tilde{\Phi}(\alpha) = \alpha$ .*

Therefore, to have the form (27), we know that at least  $\beta$  (or perhaps the function form of  $\Phi(\alpha; \beta)$  as well) must depend on the constituents. Through the example shown in the proof (Appendix A), we know that the dependence is also on the mixing ratio (i.e., the parameter  $\beta$  for a combination of materials  $A$  and  $B$  differs from that of  $C$  and  $D$  even if both  $C$  and  $D$  are mixtures of  $A$  and  $B$ ). This imposes a hard constraint to measure every pair of possible blends (for every possible mixing ratio) to establish a model; thus, we do not proceed in this direction to consider pairwise blending models.

#### 4.5 Our nonlinear blending model

The design of our blending model boils down to the design of the  $F$  map, with the three Herschel-Bulkley parameters ( $\sigma_Y$ ,  $\eta$ , and  $h$ ) as its arguments. We show later that by blending the three parameters in a nonlinear manner, it becomes possible to reproduce fascinating characteristics (as in Fig. 1) that are impossible to describe when only considering blending for effective viscosity (i.e., the blending of viscosity for each particular shear rate).

To construct our model, we used the flow curves measured with our rheometer for five combinations of materials: honey ( $Ho^b$ )/mayo ( $My^b$ ), Japanese pork cutlet sauce ( $To^b$ )/mayo ( $My^c$ ), mustard ( $Ms^b$ )/BBQ sauce ( $Bb$ ), honey ( $Ho^c$ )/oyster sauce ( $Oy^b$ ), and Worcestershire sauce ( $Wo$ )/Japanese pork cutlet sauce ( $To$ ), all with the increments of the mixing ratio set to 10%, i.e., 0 : 100%, 10 : 90%, ..., 100 : 0%.

Because of the limited number of material samples, we limited the search space for the  $F$  map, rather than adopting a general form and fully made use of optimizations, which is an interesting future direction. Because the yield stress  $\sigma_Y$  is the only parameter related

to elasticity (it describes the limit of the elastic regime), we decided to first find a function that works to blend only the yield stress. The yield stress shows up at the low-shear-rate end of the flow curve. Specifically, we assumed the following form for calculating the blended  $\sigma_{Y,M}$  from that of the two constituents  $\sigma_{Y,A}$  and  $\sigma_{Y,B}$ :

$$\sigma_{Y,M}^p = \alpha\sigma_{Y,A}^p + (1 - \alpha)\sigma_{Y,B}^p, \quad (28)$$

where  $p$  is a parameter we are going to optimize for. As discussed in Appendix B,  $p = 0$  reduces to multiplicative blending:  $\sigma_{Y,M} = \sigma_{Y,A}^\alpha \sigma_{Y,B}^{1-\alpha}$ . By changing  $p$ , we computed the relative and absolute errors between the predicted and measured (fitted) values of  $\sigma_{Y,M}$ . As in Fig. 5 (a), both errors produced negative  $p$  as the optimizer. But since having a value of  $p < 0$  would cause undefined  $\sigma_{Y,M}$  if one of  $\sigma_{Y,A}$  and  $\sigma_{Y,B}$  is zero, we used  $p = 0$  in our model. Note that by using high-end machinery for more accurate measurements for the low-shear-rate regime would enable a finer inspection, which we leave as a future work. We also did not use water as one of the constituents, as its nearly zero viscosity behavior at the low-shear-rate regime turns out to be extremely hard to measure using our rheometer).

Next, looking at the high-shear-rate end, the flow curve in the logarithmic plot appears to be straight, with the slope characterized by the power parameter  $h$ . Thus, we tried to find a function for solely blending the  $h$  parameter. In particular, we choose the following function space

$$h_M^q = \alpha h_A^q + (1 - \alpha)h_B^q. \quad (29)$$

Like we did for the yield stress, we tested both relative and absolute errors between the predicted and measured (fitted) values of  $h$ . As in Fig. 5 (b),  $q = 0.6$  gave the smallest relative error, and  $q = 1.4$  gave the smallest absolute error. We will decide which option ( $q = 0.6$  or  $q = 1.4$ ) to use later.

Finally, we investigated a way of estimating the  $\eta$  parameter for a mixture. We found that by taking the  $h$  parameter into account, we can nicely obtain the characteristic behavior (the reduction in the effective viscosities of the blends) that was observed from the measurements; we let the  $F$  map have the form

$$F((h, \eta, \sigma_Y)^T) = (h^q, \eta^{f(h)}, \ln \sigma_Y)^T. \quad (30)$$

For the space of  $f(h)$ , we considered low order polynomials of  $h$  and  $1/h$  and tested the three forms  $a_0 + a_1h + a_2h^2$ ,  $a_{-1}/h + a_0 + a_1h$ , and  $a_{-2}/h^2 + a_{-1}/h + a_0$ . We enforced  $f(1) = c$  so that our model reduces to one of the four empirical viscosity blending models ( $c = -1$  for Bingham,  $c = -0.384$  for Refutas,  $c = 1$  for linear, and  $c = 1/3$  for Kendall and Monroe). Because we have  $q = 0.6$  and  $q = 1.4$ , we now have a total of 24 candidates. For each of these cases, we used the *absolute error* between the estimated and measured stresses as the objective function to optimize for parameters  $a_*$ <sup>1</sup>. For the optimal parameter choice of each case, we also computed the *relative error* between the estimated and measured stresses. We found that discarding models with a relative error larger than 100% resulted in discarding cases  $c = 1$  and  $c = 1/3$ , and that further selecting the

<sup>1</sup>We have also tested using the relative error as the objective function. Although this resulted in a smaller average error in general, the results do not well explain all the five cases. In contrast, our result (31) can effectively explain all the five cases, as in Fig. 6.

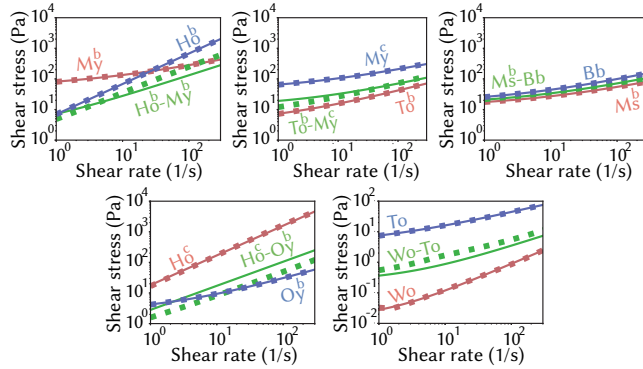


Fig. 6. The measured data (dots) and estimation from our blending model (solid lines). In each sub figure, blue and red correspond to the flow curves of pure constituents and green corresponds to half and half blending. Our model qualitatively and nicely captures the characteristic behaviors.

one with the smallest relative error resulted in  $q = 1.4$ ,  $c = -0.384$  and the following form for  $f$ :

$$f(h) = 0.116 - 3.2h + 2.7h^2. \quad (31)$$

With our model, we can estimate the Herschel-Bulkley parameters for the mixtures we tested in an average of 55% relative error. Considering the diversity of our materials, which cover different types of rheological properties, including polymers, suspensions, and nearly Newtonian, and considering the visual resemblance of the results (like Fig. 1), we are confident that the 55% relative error is good for the first step toward nonlinear blending. As shown in Fig. 6, we have a good qualitative match in the behavior of effective viscosity for a wide variation of shear rate ranging more than two orders of magnitude, which is impossible with linear blending.

#### 4.6 Limitations of our blending model

There are several limitations and future directions of our model. First, we have not considered the blending of elasticity; we assumed that all the materials had a bulk modulus  $\kappa = 10^6 \text{ Pa}$  and a shear modulus  $\mu = 10^5 \text{ Pa}$  in our simulation. Second, the accuracy for  $h < 0.4$ ,  $h \geq 1.0$ , and the case of extremely low and high shear rates need further investigation. We also point out that the identity law and associative law may not always hold from the perspective of rheology (e.g., suspension flows with different particle distributions). However, the fact that the model can nicely represent the captured flow curve is encouraging, implying that our  $F$  map is a good approximation. A ‘second order’ binary mixture model might be interesting as follow up work to improve accuracy. We also envision that further investigating the relation between the set of laws and the error would allow us to identify the correct set of laws and help us discuss the underlying structure of microscopic physics.

## 5 SIMULATION AND ELASTO-VISCOPLASTIC MODELING

We employ the generalized interpolation material point method [Bardehagen and Kober 2004] (the uGIMP variant with a fixed box-shaped material point extent for stability) and the affine particle-in-cell transfer [Jiang et al. 2015] (for better angular momentum preservation) to simulate the dynamics of continuum media described by the equation of motion:

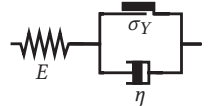
$$\rho \mathbf{a} = \nabla \cdot \boldsymbol{\sigma} + \rho \mathbf{b}, \quad (32)$$

and the mass conservation condition  $\dot{\rho} + \rho \nabla \cdot \mathbf{v} = 0$ , where,  $\rho$  is density,  $\mathbf{a} = \dot{\mathbf{v}}$  is acceleration,  $\mathbf{v}$  is the velocity,  $\mathbf{b}$  is body force, and  $\boldsymbol{\sigma}$  is the Cauchy stress tensor.

The constitutive model used for the materials follows Yue et al.’s *elastic Herschel-Bulkley model* [2015], which we briefly summarize for the completeness of material modeling, together with a few insights about its relation to purely elastic solids and Newtonian fluids.

### 5.1 1D elasto-viscoplasticity

We start with a 1D rheological model (a Maxwell-type viscoelastic model with yield stress), as in a previous study [Simo and Hughes 1998] §1.7, to sketch out the underlying concept of an elasto-viscoplastic (i.e., elastic Bingham) solid consisting of a spring (with elastic strain  $\epsilon_e$  and elastic modulus  $E$ ), dashpot (with viscoplastic strain  $\epsilon_{vp}$  and viscosity  $\eta$ ), and Coulomb friction element (with yield stress  $\sigma_Y$ ). This model is a simple illustration corresponding to the *shear* part of the 3D elasto-viscoplasticity.



For ease of presentation, we consider  $\epsilon > 0$ ,  $\epsilon_e > 0$ ,  $\epsilon_{vp} > 0$  here. The total strain  $\epsilon$  is given by  $\epsilon = \epsilon_e + \epsilon_{vp}$ , and the stress of the entire device is given by

$$\sigma = E\epsilon_e, \quad (33)$$

no matter whether the yield condition  $\sigma < \sigma_Y$  is violated. The key to elasto-viscoplasticity modeling is to appropriately *adjust* this elastic strain in such a way that the viscosity relation holds when the yield condition is violated (i.e.,  $\sigma \geq \sigma_Y$ ).

To see the above point, we write the total stress as follows when the yield condition is violated:

$$\sigma = \sigma_Y + \sigma_{ex}, \quad (34)$$

where we say the *extra stress*  $\sigma_{ex}$  is caused by the dashpot, and is given in the form  $\sigma_{ex} = \eta \dot{\epsilon}_{vp}$ . Now, by writing  $\epsilon_Y$  to represent the critical strain that gives the yield stress (i.e.,  $\sigma_Y = E\epsilon_Y$ ) and equating the two forms of stress (33) and (34), we find a relation between the elastic strain  $\epsilon_e$  and viscoplastic strain  $\epsilon_{vp}$  for  $\epsilon_e \geq \epsilon_Y$ :

$$\sigma = E\epsilon_e, \quad (35)$$

$$\dot{\epsilon}_{vp} = \frac{1}{\eta} \sigma_{ex} = \frac{1}{\eta} (\sigma - \sigma_Y) \quad (36)$$

$$\dot{\epsilon}_e = \dot{\epsilon} - \dot{\epsilon}_{vp}. \quad (37)$$

The rate of the total strain  $\dot{\epsilon}$  is caused by the effect from the outer environment; in 3D, this is caused by the velocity gradient, or in other words, the change in the deformation. This coupled relation

describes how the spring gains *excess* strain (or equivalently how the elastic strain flows into the viscoplastic strain) such that the viscous relation  $\sigma_{ex} = \eta\dot{\epsilon}_{vp}$  holds.

In the elastic Herschel-Bulkley model, the viscous response  $\sigma_{ex} = \eta\dot{\epsilon}_{vp}$  is replaced with the Herschel-Bulkley response  $\sigma_{ex} = \eta\dot{\epsilon}_{vp}^h$ ; with  $h = 1$ , we recover the standard (elastic Bingham) viscoplasticity.

## 5.2 Relation to elastic solids and Newtonian fluids

Clearly, purely elastic solids correspond to the case  $\sigma_Y \rightarrow \infty$ , because then the dashpot is ineffective and all the responses are elastic. It is also clear that for a Newtonian fluid, we must have  $\sigma_Y = 0$  to eliminate the admissible elastic regime, but we still have the choice for the elastic modulus  $E$  (reinterpret  $E$  as the shear modulus  $\mu$  in 3D). In short,  $\sigma_Y = 0$  corresponds to *visco-elasticity* (Maxwell model), and a purely Newtonian fluid is recovered when  $E \rightarrow \infty$ , which we discuss below.

Differentiating (35), substituting (37) and (36), and setting  $\sigma_Y = 0$ , we have  $\dot{\sigma} = E\dot{\epsilon} - \frac{E}{\eta}\sigma$ . Writing  $\tau = \frac{\eta}{E}$ , multiplying both sides by  $e^{\frac{t}{\tau}}$ , and rearranging, we then have  $e^{\frac{t}{\tau}}\dot{\sigma} + \frac{1}{\tau}e^{\frac{t}{\tau}}\sigma = Ee^{\frac{t}{\tau}}\dot{\epsilon}$ . Noting that the left hand side can be written as  $\frac{d}{dt}(e^{\frac{t}{\tau}}\sigma)$ , we integrate both sides and obtain  $e^{\frac{t}{\tau}}\sigma(t) - \sigma(0) = \int_0^t Ee^{\frac{t}{\tau}}\dot{\epsilon}dt$ . Assuming that we have a constant total strain rate  $\dot{\epsilon} = d$ , we have  $\int_0^t Ee^{\frac{t}{\tau}}\dot{\epsilon}dt = \eta d(e^{\frac{t}{\tau}} - 1)$ . Finally, we arrive at

$$\sigma(t) = e^{-\frac{t}{\tau}}\sigma(0) + \eta d(1 - e^{-\frac{t}{\tau}}), \quad (38)$$

where  $e^{-\frac{t}{\tau}}$  is a factor about the *memory* of the previous elastic response  $\sigma(0)$ ; thus, the model is called *history dependent* if  $\tau$  is finite. Thus,  $\tau$  can be interpreted as a time scale of relaxation, i.e., how quickly the stress approaches the limiting viscous response  $\eta d$ . As  $t \rightarrow \infty$ ,  $\sigma(t) \rightarrow \eta d$ . Now, if we take the limit of  $E \rightarrow \infty$ ,  $e^{\frac{t}{\tau}}$  quickly approaches 0 for all finite  $t > 0$ , and we have an instant viscous response  $\sigma(t) = \eta d$  (i.e., when the spring is rigid, it loses memory).

We also see that the standard Navier-Stokes equations can be recovered by plugging in the constitutive relation  $\sigma = -pI + 2\eta D$  to the equation of motion in continuum mechanics (32), together with the incompressibility condition  $\nabla \cdot \mathbf{v} = 0$ , where  $D$  is the (linearized) shear strain rate given by  $D = \frac{1}{2}(\nabla \mathbf{v} + (\nabla \mathbf{v})^T)$ .

Thus, the shear behavior of the elastic Bingham-like solid and the Newtonian viscous fluid becomes identical when  $\sigma_Y = 0$  and  $\mu \rightarrow \infty$ . For the pressure part, if  $\frac{\kappa}{\mu} \rightarrow \infty$ , the Poisson's ratio approaches 0.5, and we arrive at the incompressible case, where  $\kappa$  is the bulk modulus. Intuitively, a stiff spring means that we have a tiny nearly rigid segment attached to the dashpot, which has no effect on the dynamic behavior of the entire device. In contrast, an excessively soft spring ( $E \rightarrow 0$ ) means that we have an air parcel attached to the dashpot, making the dashpot ineffective. In summary,  $\eta$  in our model, in an elastic solid, and in a Newtonian fluid all represent the same physical concept of viscosity.

On the other hand, the above discussion suggests that we may need an elasticity blending model if we want to blend materials with different stiffness (like mayo with whipped cream). We will leave elasticity blending as future work. To investigate the effect of elasticity on our blending model, we tried different Young's moduli

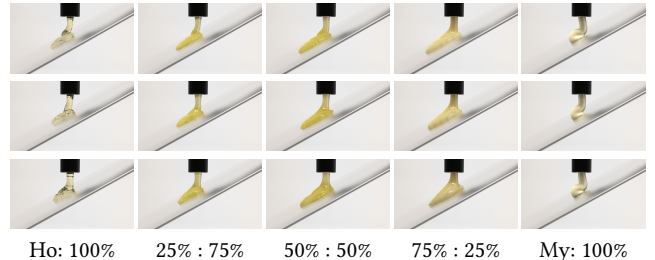


Fig. 7. The mixtures of honey (Ho) and mayo (My) at 3.4 s, simulated with different Young's modulus. From top to bottom:  $\times 0.1$ ,  $\times 1$ , and  $\times 10$  of the settings in Fig. 1.

( $\times 0.1$  and  $\times 10$ ) while fixing the Poisson's ratio and bulk and shear moduli in simulations for the honey and mayo blend example in Fig. 1. Their flowing speeds look more or less the same (as in Fig. 7), albeit a difference in the coiling frequencies. We also believe it would be interesting to consider different forms of hyperelastic energy density, in cooperation with our blending model.

## 5.3 3D elasto-viscoplasticity

Our 3D elasto-viscoplasticity model is a generalization of the 1D version, and *exactly* follows that used in Yue et al. [2015], which we summarize below for self-containedness. To describe the deformation state, we use the *deformation gradient*  $\mathbf{F}$ , which linearly maps an infinitesimal material neighborhood of an undeformed state to the corresponding deformed one [Simo and Hughes 1998]. We consider a multiplicative decomposition [Bargteil et al. 2007; Irving et al. 2004; Jones et al. 2014; Simo and Hughes 1998; Wicke et al. 2010]  $\mathbf{F} = \mathbf{F}^e \mathbf{F}^p$ , where  $\mathbf{F}^e$  and  $\mathbf{F}^p$  are the elastic and plastic components of the deformation, respectively. With the ansatz that the plasticity is volume preserving, we have  $\det(\mathbf{F}^p) = 1$ . The additive decomposition  $\boldsymbol{\epsilon} = \boldsymbol{\epsilon}_e + \boldsymbol{\epsilon}_{vp}$  we have seen in the 1D version is a linearized version of the multiplicative decomposition. When dealing with rate-dependent plastic flow for an isotropic material, it is convenient to consider the *left Cauchy-Green tensor*  $\mathbf{b} = \mathbf{F}\mathbf{F}^T$  and its elastic part  $\mathbf{b}^e = \mathbf{F}^e\mathbf{F}^{eT}$  to satisfy the objectivity (i.e., frame-indifference) for both strain and strain rate [Simo and Hughes 1998].

The elastic response of the material is described by a hyperelastic stored (or strain) energy density,

$$W = W_v(J) + W_s(\bar{\mathbf{b}}^e), \quad (39)$$

with the volumetric term  $W_v(J) = \frac{1}{2}\kappa[\frac{1}{2}(J^2 - 1) - \ln J]$  and shear term  $W_s(\bar{\mathbf{b}}^e) = \frac{1}{2}\mu(\text{Tr}[\bar{\mathbf{b}}^e] - 3)$ , where  $\kappa$  and  $\mu$  are the *bulk* and *shear* moduli,  $J = \det(\mathbf{F})$ , and  $\bar{\mathbf{b}}^e = \det(\mathbf{b}^e)^{-1/3}\mathbf{b}^e = J^{-2/3}\mathbf{b}^e$  is the *volume preserving left-Cauchy Green tensor*. The Kirchhoff stress tensor can be obtained from this stored energy density as

$$\boldsymbol{\tau} = \frac{\partial W}{\partial \mathbf{F}^e} \mathbf{F}^{eT} = \frac{\kappa}{2}(J^2 - 1)\mathbf{I} + \mu \text{dev}[\bar{\mathbf{b}}^e], \quad (40)$$

where  $\mathbf{I}$  denotes the  $3 \times 3$  identity tensor, and  $\text{dev}[\mathbf{x}] = \mathbf{x} - \frac{\text{Tr}[\mathbf{x}]}{3}\mathbf{I}$  represents the deviatoric part. The first and second terms on the right hand side of (40) describe the volumetric and shear strains,

respectively. The Kirchhoff tensor is related to the Cauchy stress via  $\sigma = \tau/J$ .

The *admissible* elastic states are defined via the *von-Mises yield condition*:

$$\Phi(s) = s - \sqrt{\frac{2}{3}}\sigma_Y \leq 0, \quad (41)$$

where  $s = \|\mathbf{s}\|_F$  is the magnitude of the shear stress  $\mathbf{s} = \text{dev}[\boldsymbol{\tau}] = \mu \text{dev}[\mathbf{b}^e]$ , and  $\sigma_Y$  is the *yield stress*. As long as the above condition is satisfied, the material remains elastic; otherwise, plastic flow occurs.

Analogous to (37), the update of the elastic part of the left Cauchy-Green tensor is given by  $\dot{\mathbf{b}}^e = \mathbf{L}\mathbf{b}^e + \mathbf{b}^e\mathbf{L}^T + \mathcal{L}_{\mathbf{v}}\mathbf{b}^e$ , where  $\mathbf{L} = \nabla\mathbf{v} = \dot{\mathbf{F}}\mathbf{F}^{-1}$  is the spatial velocity gradient and  $\mathcal{L}_{\mathbf{v}}\mathbf{b}^e$  is the Lie derivative of  $\mathbf{b}^e$  along the velocity field.  $\mathbf{L}\mathbf{b}^e + \mathbf{b}^e\mathbf{L}^T$  corresponds to the change in the total strain due to the velocity field, and the Lie derivative corresponds to the change in the plastic strain, i.e., the *plastic flow*. By applying the principle of maximum plastic dissipation to the stored energy function (39) and yield condition (41) [Simo 1988]-§1.4, one can obtain the flow rule  $\mathcal{L}_{\mathbf{v}}\mathbf{b}^e = -\frac{2}{3}\text{Tr}[\mathbf{b}^e]\dot{\gamma}\hat{\mathbf{s}}$  (see Simo and Hughes [1998]), which is a general form of (36). Defined in terms of the Lie derivative, this flow rule is objective.  $\dot{\gamma}$  is the flow rate or a scalar strain rate (we use the notation  $\dot{\gamma}$  rather than  $\gamma$  used by Yue et al. [2015] to emphasize it is a rate), and  $\hat{\mathbf{s}}$  is the flow direction. By rewriting (1) as a function of the strain rate, we obtain the following rule for the flow rate [Yue et al. 2015]:

$$\dot{\gamma}(s) = \max\left(0, \left(\frac{\Phi(s)}{\eta}\right)\right)^{1/h}. \quad (42)$$

The implementation of the update for this flow rule follows the return mapping algorithm presented by Yue et al. [2015].

#### 5.4 Determining parameters during simulation

In our simulation, we assign to each material point a vector representing the mixing ratios. Because dissolution occurs in a much longer time scale than the simulation duration for the materials we tested, we simply ignore the dissolution effect, and fixed the *initial mixing ratios*  $\alpha_p$  as a ‘label’ of the material for each material point. During the simulation, however, these material points can be spatially mixed up. Thus, we estimate the *dynamic mixing ratios* of each material point by taking the spatial average of the initial mixing ratios through the shape function. Namely, we first estimate the nodal dynamic mixing ratios  $\hat{\alpha}_i$  via

$$\hat{\alpha}_i = \frac{\sum_p V_p w_{pi} \alpha_p}{\sum_p V_p w_{pi}}, \quad (43)$$

where the particle volume  $V_p$  is used together with  $w_{pi}$  as the weight to consistently account for the blend of particles with possibly different sizes. We then compute the material point dynamic mixing ratios  $\hat{\alpha}_p$  as

$$\hat{\alpha}_p = \sum_i w_{pi} \hat{\alpha}_i. \quad (44)$$

Next, the material parameters for each material point are found using our nonlinear blending model with the material point dynamic mixing ratios  $\hat{\alpha}_p$ . We then compute the stress for each material point via (40), and the rest of the simulation steps follow the standard

Table 2. Simulation statistics. ‘cell size,’ ‘grid resolution,’ ‘domain size,’ and ‘iso-surface’ indicate the cell width and resolution of the MPM background grid, the box width of each material point used in the uGIMP formulation, and the parameter used for surface reconstruction, respectively. A frame is 1/50 second.

Example	avr min frame	#points	cell size [cm]	grid resolution	domain size [cm]	iso-surface [cm]
Nozzle experiments	1.77–3.62	2,426–137,726	0.05	110 × 76 × 60	0.025	0.015
Celery dip	5.63	136,015	0.12	66 × 36 × 66	0.12	0.036
Cup w/ spoon	4.75	118,822	0.12	63 × 55 × 63	0.12	0.09
Cup w/o spoon	4.72	122,188	0.12	63 × 55 × 63	0.12	0.09
Steak (Bb, To, Mix)	5.43	3,758–246,434	0.05	100 × 84 × 100	0.025	0.015

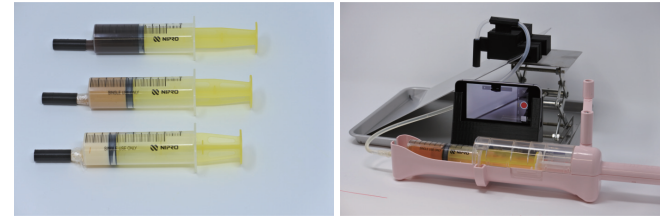


Fig. 8. We prepared our specimens in syringes (left) and used the experimental setting shown on the right to load the specimens through a nozzle.

implementation of the MPM. Note that it is possible to use the Noyes-Whitney equation [Noyes and Whitney 1897] to update the initial mixing ratios if the dissolution effect is significant.

## 6 RESULTS

All the simulations were run on an Amazon EC2 instance (c5-9xlarge, 36 cores of Intel (R) Xeon (R) Platinum 8124M 3GHz CPU). The code was parallelized using OpenMP, and each simulation used 8 cores. We did not intensively optimize our code. The statistics of the simulations are listed in Table 2, and please watch our accompanying video. To reconstruct the surface from the material points, we used a level-set-based method by Bhattacharya et al. [2015].

### 6.1 Nozzle experiment: binary mixture

Besides the nice agreement in the flow curves shown in Section 4, we conducted experiments using nozzles (Fig. 8): we loaded a specimen into a syringe and attached a silicone tube to it. The other tip of the tube was attached to a 3D printed nozzle head for position alignment. The syringe was pumped using a gear mechanism (manipulated by hand) for better control of the speed. The extruded specimen falls onto a slanted aluminum plate. The specimens were prepared by mixing two materials in the ratios 0 : 100%, 25 : 75%, 50 : 50%, 75 : 25%, and 100 : 0%, for different combinations of materials. The footage was recorded using an iPhone camera. These nozzle experiments were conducted in an air-conditioned room at 19°C, separately from the measurements using our rheometer; in Table 1, we have multiple measured data for some of the materials, and for the nozzle experiments, the material conditions (e.g., temperature) were controlled to follow those of material labels without superscripts. These are not to be confused with the materials used for deriving our blending model (in Fig. 6).

We also replicated the geometries in our simulation and compared the captured footage with our simulation. In our simulation, the

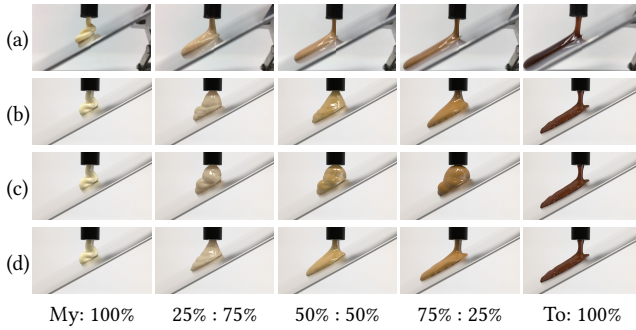


Fig. 9. Flow properties of mixtures of mayo (My) and Japanese pork cutlet sauce (To). (a) A captured footage of the mixtures with various mixing ratios. (b) MPM simulation using linearly blended material parameters. (c) A standard MPM simulation with randomized material labels. (d) MPM simulation with our nonlinear blending model.

parameters for the constituents, i.e., 0 : 100% and 100 : 0%, were taken from the measurements using our rheometer (material labels without superscripts), and those for the mixtures were computed with our blending model using the mixing ratio and parameters for the constituents.

In general, the simulated results with a linear blending approach appear to have a much more viscous behavior.

**6.1.1 Mayo and honey.** We first performed tests for the combination of mayo and honey. As shown in Fig. 1, this mixture shows a much smoother flow, as opposed to the pure mayo or pure honey, which stacks near the nozzle. This behavior was effectively captured using our nonlinear blending model, and could not be captured either by the MPM simulation using linearly blended material parameters or by initializing the material points using randomized binary labels (for mayo and honey) and computing the stress by summing the per-particle stress computed using parameters for the constituents (we call the latter the standard MPM hereafter).

**6.1.2 Mayo and Japanese pork cutlet sauce.** Next, we performed tests for the combination of mayo and Japanese port cutlet sauce. Like the combination of honey and mayo, the mixed materials flow smoothly, whereas linearly blending material parameters and the standard MPM simulation with randomized material labels failed to capture this behavior. (Fig. 10).

**6.1.3 Oyster sauce and honey.** We then conducted tests for the combination of oyster sauce and honey (Fig. 10). Again, we observed that with linearly blended material parameters or the standard MPM simulation with randomized material labels, the flows of the intermediate mixing ratios were much slower than the actual footage. Our nonlinear blending model captured faster flow. We also observed a mismatch between the simulated and captured examples for the 50 : 50% blend, 75 : 25% blend, and pure oyster sauce. We believe this is due to the lack of surface tension in our simulation. The pure oyster sauce flowed down the slope without spreading in the transverse direction, whereas the simulated one did due to the absence of surface tension. We leave the incorporation of surface tension as future work since viscosity treatment was our main focus.

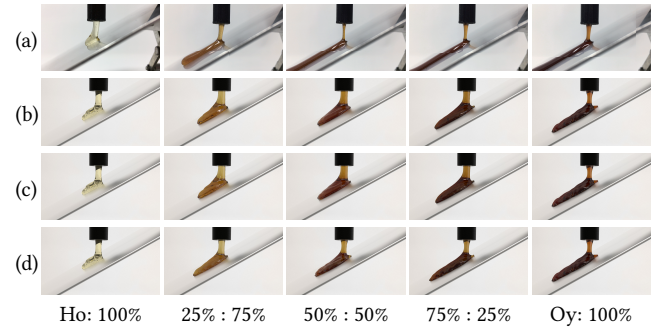


Fig. 10. Blending honey (Ho) and oyster sauce (Oy). (a) A captured footage of the mixtures with various mixing ratios. (b) MPM simulation using linearly blended material parameters. (c) A standard MPM simulation with randomized material labels. (d) MPM simulation with our nonlinear blending model.

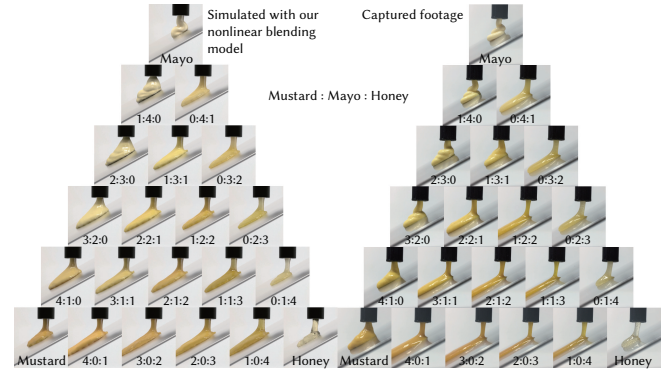


Fig. 11. Mixture of three different materials: mayo (My), mustard (Ms), and honey (Ho). Left: simulated with our nonlinear blending model. Right: captured footage from our experiment.

## 6.2 Nozzle experiment: mixture of three materials

We also tested our model for mixtures of three materials, mustard, mayo, and honey. These three materials are the typical constituents of a honey mustard sauce. The space of the mixture forms a triangle, as in Fig. 11, and this example exemplifies a simple blend-of-blend case. The geometric settings of the experiments follow those in the previous section. In our simulation, the material parameters of the mixtures were estimated from only the three constituents, and our model worked well for this mixture of three materials.

## 6.3 Celery dip

Encouraged by the nozzle experiments, we applied our model to more realistic situations. First, we simulated celery being dipped into mayo, mustard, and a half-and-half mixture with a linear blending approach<sup>2</sup> and with our nonlinear blending model. The ‘thickness’ of the sauces and their differences were nicely captured with our model, but the linear blending resulted in a more viscous behavior.

<sup>2</sup>The standard MPM simulation with randomized material labels.

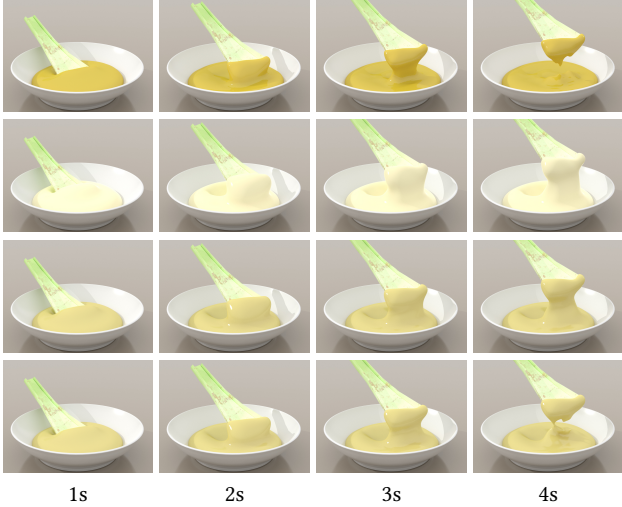


Fig. 12. Celery dips. From top to bottom: pure mustard (Ms), pure mayo (My), half-and-half mixture (linear blending), and half-and-half mixture (our model).

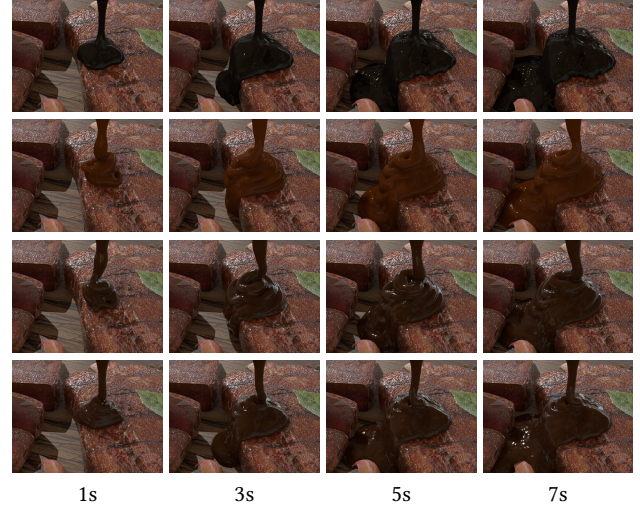


Fig. 14. Steak. From top to bottom: Japanese port cutlet sauce (To), BBQ sauce (Bb), half-and-half mixture (linear blending), and half-and-half mixture (our model).

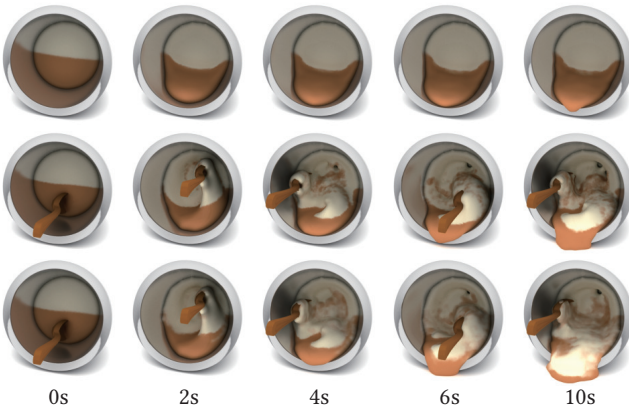


Fig. 13. We assigned the mayo (My) material to the white part and the honey (Ho) material to the brown part. Top: without interaction, the fluid flows slowly. Middle and bottom: a spoon was used to blend the materials with a linear blending (middle) and our model (bottom). The results with our model exhibit a dynamic and less viscous flow.

#### 6.4 Mixing in a cup with spoon

We prepared a fluid initially consisting of two different material regions, the white part was assigned to the mayo material and the brown part to the honey material (as in Fig. 13). Without interaction, the fluid flows slowly. Blending with a spoon and using our nonlinear blending model, the fluid looks less viscous and exhibits interesting dynamics. With the linear blending approach<sup>2</sup>, the fluid appears to be more viscous than the results using our nonlinear model.

#### 6.5 Steak

Finally, we pured three types of sauces onto a steak, i.e., Japanese port cutlet sauce, BBQ sauce, and half-and-half mixtures with the linear blending approach<sup>2</sup> and with our nonlinear blending model. The Japanese pork cutlet sauce was more like a fluid; it landed on the steak straight and flowed the most smoothly. The BBQ sauce was more viscous and had a much higher yield stress; it came down intermittently at the beginning then started to coil slowly afterwards. The half-and-half mixture with our nonlinear model flowed more smoothly compared to the BBQ sauce, and coiled stably, while that with the linear blending approach<sup>2</sup> again exhibited a more viscous behavior.

### 7 CONCLUSIONS AND FUTURE WORK

By using a rheometer, we measured the flow curves of various fluid-like foods and their mixtures, and found that the Herschel-Bulkley model could nicely represent these flow curves. Thus, it is expected that the material properties of the mixtures also live in the space of the Herschel-Bulkley model. By studying the laws of blending and the general function forms of blending (18), we constructed a nonlinear blending model (30) that produces materials inside the space of the Herschel-Bulkley model, and nicely captures the intriguing and unintuitive behaviors of the blends.

The elastic Herschel-Bulkley model used to simulate our materials consists of rate-dependent viscosity, yield stress, and elasticity (§ 5.1), and this combination covers many interesting daily materials, those we want to reproduce in graphics (setting the yield stress to zero also recovers Maxwell-type viscoelastic materials). Our methodology targets on such materials and potentially has a wider application than what we have covered in the paper. But even with the materials we tested, they have a quite different underlying microscopic physics (emulsions, polymers, colloidal suspensions, etc).

Besides the immediate benefit of our research on simulating dynamical mixing of multiple fluids (e.g. for cooking), our model can provide a nice initial guess for the material property of an unmeasured mixture with known parameters. Having done measurements with the rheometer for several materials, we learned of certain limitations. First, a rheometer with a practical accuracy (like ours) is expensive (\$50k), second, the measurement can be time-consuming, and most importantly, the combinatorial explosion of measurements for mixtures is likely unrealistic. With our model, practitioners without the availability to measure the viscous relations of mixtures are able to make their own simulations of mixture by only knowing the material parameters of the constituents, keeping the list of the necessary material parameters finite and minimum. We believe that our model will provide the opportunity to generate various interesting viscoplastic animations with a variety of mixtures.

There are several future directions to extend our research. First, it would be interesting to study how elasticity can be blended in a mixture. Second, we are willing to study a wider range of materials including  $h < 0.3$ ,  $h \geq 1.0$ , and cases of extremely low and high shear rates, as well as mixtures that do not follow the laws of blending. It would be interesting to study how a secondary binary mixture model can help increase estimation accuracy. Temperature dependency, chemical reactions, elasticity blending (including the influence of the choice of the hyperelastic stored energy density), and optical blending are equally important to investigate for future work.

## ACKNOWLEDGMENTS

We thank anonymous reviewers, Yuki Yoshida, and Hirotaka Sakamoto for insightful suggestions and discussions, and Louisa Andersen for her help in producing the video. This work was supported in part by JSPS Grant-in-Aid for Young Scientists (A) 17H04682, and JSPS Grant-in-Aid for Scientific Research on Innovative Areas 18H05001.

## REFERENCES

- American Society for Testing and Materials 2016. *ASTM D7152 11: Standard Practice for Calculating Viscosity of a Blend of Petroleum Products*. American Society for Testing and Materials.
- Ryoichi Ando, Nils Thürey, and Chris Wojtan. 2013. Highly Adaptive Liquid Simulations on Tetrahedral Meshes. *ACM Transactions on Graphics (Proc. of SIGGRAPH 2013)* 32, 4 (2013), 103:1–103:10. <https://doi.org/10.1145/2461912.2461982>
- Svante Arrhenius. 1887. Über die Dissociation der in Wasser gelösten Stoffe. *Zeitschrift für Physikalische Chemie* 1U, 1 (1887), 631–648.
- Fabio Bacchini, Vyacheslav Olshevsky, Stefaan Poedts, and Giovanni Lapenta. 2017. A new Particle-in-Cell method for modeling magnetized fluids. *Computer Physics Communications* 210 (2017), 79–91. <https://doi.org/10.1016/j.cpc.2016.10.001>
- Scott G. Bardenhagen and Edward M. Kober. 2004. The Generalized Interpolation Material Point Method. *CMES: Computer Modeling in Engineering and Sciences* 5, 6 (2004), 477–495.
- Adam W. Bargteil, Chris Wojtan, Jessica K. Hodgins, and Greg Turk. 2007. A Finite Element Method for Animating Large Viscoplastic Flow. *ACM Transactions on Graphics (Proc. of SIGGRAPH 2007)* 26, 3 (2007), 16:1–8. <https://doi.org/10.1145/1276377.1276397>
- Héctor Barreiro, Ignacio García-Fernández, Iván Alduán, and Miguel A. Otaduy. 2017. Conformation Constraints for Efficient Viscoelastic Fluid Simulation. *ACM Transactions on Graphics (Proc. of SIGGRAPH Asia 2017)* 36, 6 (2017), 221:1–11. <https://doi.org/10.1145/3130800.3130854>
- Christopher Batty, Florence Bertails, and Robert Bridson. 2007. A Fast Variational Framework for Accurate Solid-fluid Coupling. *ACM Transactions on Graphics (Proc. of SIGGRAPH 2007)* 26, 3 (2007), 100:1–7. <https://doi.org/10.1145/1276377.1276502>
- Christopher Batty, Andres Uribe, Basile Audoly, and Eitan Grinspun. 2012. Discrete Viscous Sheets. *ACM Transactions on Graphics (Proc. of SIGGRAPH Asia 2012)* 31, 4 (2012), 113:1–7. <https://doi.org/10.1145/2185520.2185609>
- Markus Becker, Markus Ihmsen, and Matthias Teschner. 2009. Corotated SPH for Deformable Solids. In *Eurographics Workshop on Natural Phenomena*, Eric Galin and Jens Schneider (Eds.). The Eurographics Association, 27–34. <https://doi.org/10.2312/EG/DL/conf/EG2009/nph/027-034>
- Markus Becker and Matthias Teschner. 2007. Weakly Compressible SPH for Free Surface Flows. In *Proceedings of the 2007 ACM SIGGRAPH/Eurographics Symposium on Computer Animation (SCA '07)*. Eurographics Association, Aire-la-Ville, Switzerland, Switzerland, 209–217. <http://dl.acm.org/citation.cfm?id=1272690.1272719>
- Jan Bender and Dan Koschier. 2015. Divergence-free Smoothed Particle Hydrodynamics. In *Proceedings of the 14th ACM SIGGRAPH / Eurographics Symposium on Computer Animation (SCA '15)*. ACM, New York, NY, USA, 147–155. <https://doi.org/10.1145/2786784.2786796>
- Miklós Bergou, Basile Audoly, Etienne Vouga, Max Wardetzky, and Eitan Grinspun. 2010. Discrete Viscous Threads. *ACM Transactions on Graphics (Proc. of SIGGRAPH 2010)* 29, 4 (2010), 116:1–10. <https://doi.org/10.1145/1778765.1778853>
- Haimasree Bhattacharya, Yue Gao, and Adam W. Bargteil. 2015. A Level-Set Method for Skinning Animated Particle Data. *IEEE Transactions on Visualization and Computer Graphics* 21, 3 (March 2015), 315–327. <https://doi.org/10.1109/TVCG.2014.2362546>
- Eugene C. Bingham and Delbert F. Brown. 1932. The Mixture Law. *Journal of Rheology* 3, 1 (1932), 95–112. <https://doi.org/10.1122/1.2116447>
- Tyson Brochu, Christopher Batty, and Robert Bridson. 2010. Matching Fluid Simulation Elements to Surface Geometry and Topology. *ACM Transactions on Graphics (Proc. of SIGGRAPH 2010)* 29, 4 (2010), 47:1–9. <https://doi.org/10.1145/1778765.1778784>
- John W. Cahn and John E. Hilliard. 1958. Free Energy of a Nonuniform System. I. Interfacial Free Energy. *The Journal of Chemical Physics* 28, 2 (1958), 258–267. <https://doi.org/10.1063/1.1744102>
- Mark Carlson, Peter J. Mucha, and Greg Turk. 2004. Rigid Fluid: Animating the Interplay Between Rigid Bodies and Fluid. *ACM Transactions on Graphics (Proc. of SIGGRAPH 2004)* 23, 3 (2004), 377–384. <https://doi.org/10.1145/1015706.1015733>
- Mark Carlson, Peter J. Mucha, R. Brooks Van Horn, III, and Greg Turk. 2002. Melting and Flowing. In *Proceedings of the 2002 ACM SIGGRAPH/Eurographics Symposium on Computer Animation (SCA '02)*. ACM, New York, NY, USA, 167–174. <https://doi.org/10.1145/545261.545289>
- Pierre J. Carreau. 1972. Rheological Equations from Molecular Network Theories. *Transactions of the Society of Rheology* 16, 1 (1972), 99–127. <https://doi.org/10.1122/1.549276>
- Yuanzhang Chang, Kai Bao, Youquan Liu, Jian Zhu, and Enhua Wu. 2009. A Particle-based Method for Viscoelastic Fluids Animation. In *Proceedings of the 16th ACM Symposium on Virtual Reality Software and Technology (VRST '09)*. ACM, 111–117. <https://doi.org/10.1145/1643928.1643954>
- Pascal Clausen, Martin Wicke, Jonathan R. Shewchuk, and James F. O'Brien. 2013. Simulating Liquids and Solid-liquid Interactions with Lagrangian Meshes. *ACM Transactions on Graphics* 32, 2 (2013), 17:1–15. <https://doi.org/10.1145/2451236.2451243>
- Simon Clavet, Philippe Beaudoin, and Pierre Poulin. 2005. Particle-based Viscoelastic Fluid Simulation. In *Proceedings of the 2005 ACM SIGGRAPH/Eurographics Symposium on Computer Animation (SCA '05)*. ACM, New York, NY, USA, 219–228. <https://doi.org/10.1145/1073368.1073400>
- Paul W. Cleary, Soon Hyoung Pyo, Mahesh Prakash, and Bon Ki Koo. 2007. Bubbling and Frothing Liquids. *ACM Transactions on Graphics (Proc. of SIGGRAPH 2007)* 26, 3 (2007), 97:1–6. <https://doi.org/10.1145/1276377.1276499>
- Peter A. Cundall and Otto D. L. Strack. 1979. A discrete numerical model for granular assemblies. *Géotechnique* 29, 1 (1979), 47–65.
- Gilles Daviet and Florence Bertails-Descoubes. 2016. A Semi-implicit Material Point Method for the Continuum Simulation of Granular Materials. *ACM Transactions on Graphics (Proc. of SIGGRAPH 2016)* 35, 4 (2016), 102:1–13. <https://doi.org/10.1145/2897824.2925877>
- Daniel C. Drucker and William Prager. 1952. Soil mechanics and plastic analysis for limit design. *Quart. Appl. Math.* 10, 2 (1952), 157–165.
- Sachith Dunatunga and Ken Kamrin. 2015. Continuum modelling and simulation of granular flows through their many phases. *Journal of Fluid Mechanics* 779 (2015), 483–513.
- Douglas Enright, Stephen Marschner, and Ronald Fedkiw. 2002. Animation and Rendering of Complex Water Surfaces. *ACM Transactions on Graphics (Proc. of SIGGRAPH 2002)* 21, 3 (2002), 736–744. <https://doi.org/10.1145/566654.566645>
- Yu Fang, Yuanming Hu, Shi-Min Hu, and Chenfanfu Jiang. 2018. A Temporally Adaptive Material Point Method with Regional Time Stepping. *Computer Graphics Forum* 37, 8 (2018), 195–204. <https://doi.org/10.1111/cgf.13524>
- Florian Ferstl, Ryoichi Ando, Chris Wojtan, Rüdiger Westermann, and Nils Thuerey. 2016. Narrow Band FLIP for Liquid Simulations. *Computer Graphics Forum* 35, 2 (2016), 225–232. <https://doi.org/10.1111/cgf.12825>
- Nick Foster and Ronald Fedkiw. 2001. Practical Animation of Liquids. In *Proceedings of the 28th Annual Conference on Computer Graphics and Interactive Techniques (SIGGRAPH '01)*. ACM, New York, NY, USA, 23–30. <https://doi.org/10.1145/383259.383261>

- Nick Foster and Dimitri Metaxas. 1996. Realistic Animation of Liquids. *Graphical Models and Image Processing* 58, 5 (1996), 471–483. <https://doi.org/10.1006/gmip.1996.0039>
- Chuyuan Fu, Qi Guo, Theodore Gast, Chenfanfu Jiang, and Joseph Teran. 2017. A Polynomial Particle-in-cell Method. *ACM Transactions on Graphics (Proc. of SIGGRAPH Asia 2017)* 36, 6 (2017), 222:1–12. <https://doi.org/10.1145/3130800.3130878>
- Ming Gao, Andre Pradhana, Xuchen Han, Qi Guo, Grant Kot, Eftychios Sifakis, and Chenfanfu Jiang. 2018. Animating Fluid Sediment Mixture in Particle-laden Flows. *ACM Transactions on Graphics (Proc. of SIGGRAPH 2018)* 37, 4 (2018), 149:1–11. <https://doi.org/10.1145/3197517.3201309>
- Ming Gao, Andre Pradhana, Chenfanfu Jiang, and Eftychios Sifakis. 2017. An Adaptive Generalized Interpolation Material Point Method for Simulating Elastoplastic Materials. *ACM Transactions on Graphics (Proc. of SIGGRAPH Asia 2017)* 36, 6 (2017), 223:1–12. <https://doi.org/10.1145/3130800.3130879>
- Ming Gao, Xinlei Wang, Kui Wu, Andre Pradhana, Eftychios Sifakis, Cem Yuksel, and Chenfanfu Jiang. 2018. GPU Optimization of Material Point Methods. *ACM Transactions on Graphics (Proc. of SIGGRAPH Asia 2018)* 37, 6 (2018), 254:1–12. <https://doi.org/10.1145/3272127.3275044>
- Dan Gerszewski, Haimasree Bhattacharya, and Adam W. Bargteil. 2009. A Point-based Method for Animating Elastoplastic Solids. In *Proceedings of the 2009 ACM SIGGRAPH/Eurographics Symposium on Computer Animation (SCA '09)*. ACM, 133–138. <https://doi.org/10.1145/1599470.1599488>
- Tolga G. Goktekin, Adam W. Bargteil, and James F. O'Brien. 2004. A Method for Animating Viscoelastic Fluids. *ACM Transactions on Graphics (Proc. of SIGGRAPH 2004)* 23, 3 (2004), 463–468. <https://doi.org/10.1145/1015706.1015746>
- Xiaowei He, Huamin Wang, and Enhua Wu. 2018. Projective Peridynamics for Modeling Versatile Elastoplastic Materials. *IEEE Transactions on Visualization and Computer Graphics* 24, 9 (2018), 2589–2599. <https://doi.org/10.1109/TVCG.2017.2755646>
- Winslow H. Herschel and Ronald Bulkley. 1926. Konsistenzmessungen von Gummi-Benzollösungen. *Kolloid-Zeitschrift & Zeitschrift für Polymere* 39, 4 (1926), 291–300.
- Jeong-Mo Hong and Chang-Hun Kim. 2005. Discontinuous Fluids. *ACM Transactions on Graphics (Proc. of SIGGRAPH 2005)* 24, 3 (2005), 915–920. <https://doi.org/10.1145/1073204.1073283>
- Yuanming Hu, Yu Fang, Ziheng Ge, Ziyin Qu, Yixin Zhu, Andre Pradhana, and Chenfanfu Jiang. 2018. A Moving Least Squares Material Point Method with Displacement Discontinuity and Two-way Rigid Body Coupling. *ACM Transactions on Graphics (Proc. of SIGGRAPH 2018)* 37, 4 (2018), 150:1–14. <https://doi.org/10.1145/3197517.3201293>
- Markus Ihmsen, Jens Cornelis, Barbara Solenthaler, Christopher Horvath, and Matthias Teschner. 2014. Implicit Incompressible SPH. *IEEE Transactions on Visualization and Computer Graphics* 20, 3 (March 2014), 426–435. <https://doi.org/10.1109/TVCG.2013.105>
- Geoffrey Irving, Joseph M. Teran, and Ronald P. Fedkiw. 2004. Invertible Finite Elements for Robust Simulation of Large Deformation. In *Proceedings of the 2004 ACM SIGGRAPH/Eurographics Symposium on Computer Animation (SCA '04)*. Eurographics Association, 131–140. <https://doi.org/10.1145/1028523.1028541>
- Chenfanfu Jiang, Theodore Gast, and Joseph Teran. 2017. Anisotropic Elastoplasticity for Cloth, Knit and Hair Frictional Contact. *ACM Transactions on Graphics (Proc. of SIGGRAPH 2017)* 36, 4 (2017), 152:1–14. <https://doi.org/10.1145/3072959.3073623>
- Chenfanfu Jiang, Craig Schroeder, Andrew Selle, Joseph Teran, and Alexey Stomakhin. 2015. The Affine Particle-in-cell Method. *ACM Transactions on Graphics (Proc. of SIGGRAPH 2015)* 34, 4 (2015), 51:1–10. <https://doi.org/10.1145/2766996>
- Chenfanfu Jiang, Craig Schroeder, Joseph Teran, Alexey Stomakhin, and Andrew Selle. 2016. The Material Point Method for Simulating Continuum Materials. In *ACM SIGGRAPH 2016 Courses (SIGGRAPH '16)*. ACM, New York, NY, USA, Article 24, 52 pages. <https://doi.org/10.1145/2897826.2927348>
- Ben Jones, Stephen Ward, Ashok Jallepalli, Joseph Pereria, and Adam W. Bargteil. 2014. Deformation Embedding for Point-based Elastoplastic Simulation. *ACM Transactions on Graphics* 33, 2 (2014), 21:1–9. <https://doi.org/10.1145/2560795>
- Harry C. Jones and Eugene C. Bingham. 1905. Conductivity and viscosity of solutions of certain salts in mixtures of acetone with methyl alcohol, with ethyl alcohol and water. *American Chemical Journal* 34 (1905), 481–554.
- James Kendall and Kenneth Potter Monroe. 1917. THE VISCOSITY OF LIQUIDS. II. THE VISCOSITY-COMPOSITION CURVE FOR IDEAL LIQUID MIXTURES. I. *Journal of the American Chemical Society* 39, 9 (1917), 1787–1802. <https://doi.org/10.1021/ja02254a001>
- Byungmoon Kim. 2010. Multi-phase Fluid Simulations Using Regional Level Sets. *ACM Transactions on Graphics (Proc. of SIGGRAPH Asia 2010)* 29, 6 (2010), 175:1–8.
- Gergely Klár, Theodore Gast, Chuyuan Fu, Craig Schroeder, Chenfanfu Jiang, and Joseph Teran. 2016. Drucker-prager Elastoplasticity for Sand Animation. *ACM Transactions on Graphics (Proc. of SIGGRAPH 2016)* 35, 4 (2016), 103:1–12. <https://doi.org/10.1145/2897824.2925906>
- Egor Larionov, Christopher Batty, and Robert Bridson. 2017. Variational Stokes: A Unified Pressure-viscosity Solver for Accurate Viscous Liquids. *ACM Transactions on Graphics (Proc. of SIGGRAPH 2017)* 36, 4 (2017), 101:1–11. <https://doi.org/10.1145/3072959.3073628>
- E. L. Lederer. 1931. Zur Theorie der Viskosität von Flüssigkeiten. *Kolloid Beihefte* 34, 5–9 (1931), 270–338. <https://doi.org/10.1007/BF02556584>
- Toon Lenaerts, Bart Adams, and Philip Dutré. 2008. Porous Flow in Particle-based Fluid Simulations. *ACM Transactions on Graphics (Proc. of SIGGRAPH 2008)* 27, 3 (2008), 49:1–8. <https://doi.org/10.1145/1360612.1360648>
- Frank Losasso, Geoffrey Irving, Eran Guendelman, and Ronald Fedkiw. 2006a. Melting and burning solids into liquids and gases. *IEEE Transactions on Visualization and Computer Graphics* 12, 3 (2006), 343–352. <https://doi.org/10.1109/TVCG.2006.51>
- Frank Losasso, Tamar Shinar, Andrew Selle, and Ronald Fedkiw. 2006b. Multiple Interacting Liquids. *ACM Transactions on Graphics (Proc. of SIGGRAPH 2006)* 25, 3 (2006), 812–819.
- Miles Macklin and Matthias Müller. 2013. Position Based Fluids. *ACM Transactions on Graphics (Proc. of SIGGRAPH 2013)* 32, 4 (2013), 104:1–12. <https://doi.org/10.1145/2461912.2461984>
- Hai Mao and Yee-Hong Yang. 2006. Particle-based Immiscible Fluid-fluid Collision. In *Proceedings of Graphics Interface 2006 (GI '06)*. Canadian Information Processing Society, Toronto, Ont., Canada, Canada, 49–55. <http://dl.acm.org/citation.cfm?id=1143079.1143088>
- Marek Krzysztof Misztal, Kenny Erleben, Adam Bargteil, Jens Fursund, Brian Bunch Christensen, Jakob Andreas Bærentzen, and Robert Bridson. 2014. Multiphase Flow of Immiscible Fluids on Unstructured Moving Meshes. *IEEE Transactions on Visualization and Computer Graphics* 20, 1 (2014), 4–16. <https://doi.org/10.1109/TVCG.2013.97>
- Georgios Moutsanidis, David Kamensky, Duan Z. Zhang, Yuri Bazilevs, and Christopher C. Long. 2019. Modeling strong discontinuities in the material point method using a single velocity field. *Computer Methods in Applied Mechanics and Engineering* 345 (2019), 584–601. <https://doi.org/10.1016/j.cma.2018.11.005>
- Matthias Müller, David Charypar, and Markus Gross. 2003. Particle-based Fluid Simulation for Interactive Applications. In *Proceedings of the 2003 ACM SIGGRAPH/Eurographics Symposium on Computer Animation (SCA '03)*. Eurographics Association, Aire-la-Ville, Switzerland, Switzerland, 154–159. <http://dl.acm.org/citation.cfm?id=846276.846298>
- Matthias Müller, Bruno Heidelberger, Marcus Hennix, and John Ratcliff. 2007. Position based dynamics. *Journal of Visual Communication and Image Representation* 18, 2 (2007), 109–118. <https://doi.org/10.1016/j.jvcir.2007.01.005>
- Matthias Müller, Simon Schirrm, Matthias Teschner, Bruno Heidelberger, and Markus Gross. 2004. Interaction of Fluids with Deformable Solids: Research Articles. *Computer Animation and Virtual Worlds* 15, 3–4 (July 2004), 159–171. <https://doi.org/10.1002/cav.153/4>
- Matthias Müller, Barbara Solenthaler, Richard Keiser, and Markus Gross. 2005. Particle-based Fluid-fluid Interaction. In *Proceedings of the 2005 ACM SIGGRAPH/Eurographics Symposium on Computer Animation (SCA '05)*. ACM, New York, NY, USA, 237–244. <https://doi.org/10.1145/1073368.1073402>
- Rahul Narain, Abhinav Golas, and Ming C. Lin. 2010. Free-flowing Granular Materials with Two-way Solid Coupling. *ACM Transactions on Graphics (Proc. of SIGGRAPH Asia 2010)* 29, 6 (2010), 173:1–10. <https://doi.org/10.1145/1882261.1866195>
- Arthur A. Noyes and Willis R. Whitney. 1897. The rate of solution of solid substances in their own sultutions. *Journal of the American Chemical Society* 19, 12 (1897), 930–934. <https://doi.org/10.1021/ja02086003>
- James G. Oldroyd and Alan Herries Wilson. 1950. On the formulation of rheological equations of state. *Proceedings of the Royal Society of London. Series A. Mathematical and Physical Sciences* 200, 1063 (1950), 523–541. <https://doi.org/10.1098/rspa.1950.0035>
- Afonso Paiva, Fabiano Petronetto, Thomas Lewiner, and Geovan Tavares. 2006. Particle-based non-newtonian fluid animation for melting objects. In *Proceedings of XIX Brazilian Symposium on Computer Graphics and Image Processing (SIBGRAPI'06) (SIBGRAPI'06)*, 78–85.
- Afonso Paiva, Fabiano Petronetto, Thomas Lewiner, and Geovan Tavares. 2009. Particle-based viscoplastic fluid/solid simulation. *Computer-Aided Design* 41, 4 (2009), 306–314. <https://doi.org/10.1016/j.cad.2008.10.004> Point-based Computational Techniques.
- Jinho Park, Younghwi Kim, Daehyeon Wi, Nahyup Kang, Sung Yong Shin, and Junyoung Noh. 2008. A Unified Handling of Immiscible and Miscible Fluids. *Computer Animation and Virtual Worlds* 19, 3–4 (2008), 455–467. <https://doi.org/10.1002/cav.19:3/4>
- Andreas Peer, Markus Ihmsen, Jens Cornelis, and Matthias Teschner. 2015. An Implicit Viscosity Formulation for SPH Fluids. *ACM Transactions on Graphics (Proc. of SIGGRAPH 2015)* 34, 4 (2015), 114:1–10. <https://doi.org/10.1145/2766925>
- Andre Pradhana. 2017. *Multiphase Simulation Using Material Point Method*. dissertation. UCLA. <https://escholarship.org/uc/item/52bb82q>
- Andre Pradhana, Theodore Gast, Gergely Klár, Chuyuan Fu, Joseph Teran, Chenfanfu Jiang, and Ken Museth. 2017. Multi-species Simulation of Porous Sand and Water Mixtures. *ACM Transactions on Graphics (Proc. of SIGGRAPH 2017)* 36, 4 (2017), 105:1–11. <https://doi.org/10.1145/3072959.3073651>
- Daniel Ram, Theodore Gast, Chenfanfu Jiang, Craig Schroeder, Alexey Stomakhin, Joseph Teran, and Pirouz Kavehpour. 2015. A Material Point Method for Viscoelastic

- Fluids, Foams and Sponges. In *Proceedings of the 14th ACM SIGGRAPH / Eurographics Symposium on Computer Animation (SCA '15)*. ACM, 157–163. <https://doi.org/10.1145/2786784.2786798>
- Bo Ren, Chenfeng Li, Xiao Yan, Ming C. Lin, Javier Bonet, and Shi-Min Hu. 2014. Multiple-Fluid SPH Simulation Using a Mixture Model. *ACM Transactions on Graphics* 33, 5 (2014), 171:1–11. <https://doi.org/10.1145/2645703>
- Avi Robinson-Mosher, Tamar Shinar, Jon Gretarsson, Jonathan Su, and Ronald Fedkiw. 2008. Two-way Coupling of Fluids to Rigid and Deformable Solids and Shells. *ACM Transactions on Graphics (Proc. of SIGGRAPH 2008)* 27, 3 (2008), 46:1–9. <https://doi.org/10.1145/1360612.1360645>
- Michel (Sr) Roegiers and Lucien Roegiers. 1946. La viscosité des mélanges de fluides normaux. (1946).
- Michael Rusin. 1975. The Structure of Nonlinear Blending Models. *Chemical Engineering Science* 30, 8 (1975), 937–944.
- Alireza Sadeghirad, Rebecca M. Brannon, and Jeff Burghardt. 2011. A convected particle domain interpolation technique to extend applicability of the material point method for problems involving massive deformations. *Internat. J. Numer. Methods Engrg.* 86, 12 (2011), 1435–1456. <https://doi.org/10.1002/nme.3110>
- Seung-Ho Shin, Hyeong Ryel Kam, and Chang-Hun Kim. 2010. Hybrid Simulation of Miscible Mixing with Viscous Fingering. *Computer Graphics Forum (Proc. EUROGRAPHICS 2010)* 29, 2 (2010), 675–683.
- J. C. Simo. 1988. A Framework for Finite Strain Elastoplasticity Based on Maximum Plastic Dissipation and the Multiplicative Decomposition: Part I. Continuum Formulation. *Computer Methods in Applied Mechanics and Engineering* 66, 2 (feb 1988), 199–219.
- Juan C. Simo and Thomas J. R. Hughes. 1998. *Computational Inelasticity*. Springer.
- Barbara Solenthaler and Renato B. Pajarola. 2009. Predictive-corrective Incompressible SPH. *ACM Transaction on Graphics (Proc. of SIGGRAPH 2009)* 28, 3 (2009), 40:1–6. <https://doi.org/10.1145/1531326.1531346>
- Barbara Solenthaler, Jürg Schläfli, and Renato Pajarola. 2007. A unified particle model for fluid–solid interactions. *Computer Animation and Virtual Worlds* 18, 1 (2007), 69–82. <https://doi.org/10.1002/cav.162>
- Jos Stam. 1999. Stable Fluids. In *Proceedings of the 26th Annual Conference on Computer Graphics and Interactive Techniques (SIGGRAPH '99)*. ACM Press/Addison-Wesley Publishing Co., New York, NY, USA, 121–128. <https://doi.org/10.1145/311535.311548>
- Alexey Stomakhin, Craig Schroeder, Lawrence Chai, Joseph Teran, and Andrew Selle. 2013. A Material Point Method for Snow Simulation. *ACM Transactions on Graphics (Proc. of SIGGRAPH 2013)* 32, 4 (2013), 102:1–10. <https://doi.org/10.1145/2461912.2461948>
- Alexey Stomakhin, Craig Schroeder, Chenfanfu Jiang, Lawrence Chai, Joseph Teran, and Andrew Selle. 2014. Augmented MPM for phase-change and varied materials. *ACM Transactions on Graphics (Proc. of SIGGRAPH 2014)* 33, 4 (2014), 138:1–11.
- Deborah Sulsky, Zhen Chen, and Howard L. Schreyer. 1994. A particle method for history-dependent materials. *Computer methods in applied mechanics and engineering* 118, 1 (1994), 179–196.
- Deborah Sulsky, Shi-Jian Zhou, and Howard L. Schreyer. 1995. Application of a particle-in-cell method to solid mechanics. *Computer Physics Communications* 87, 1–2 (1995), 236–252.
- Demetri Terzopoulos and Kurt Fleischer. 1988. Modeling Inelastic Deformation: Viscoelasticity, Plasticity, Fracture. *SIGGRAPH Computer Graphics (Proc. of SIGGRAPH 1988)* 22, 4 (1988), 269–278. <https://doi.org/10.1145/378456.378522>
- Martin Wicke, Daniel Ritchie, Bryan M. Klingner, Sebastian Burke, Jonathan R. Shewchuk, and James F. O'Brien. 2010. Dynamic Local Remeshing for Elastoplastic Simulation. *ACM Transactions on Graphics (Proc. of SIGGRAPH 2010)* 29, 4 (2010), 49:1–11. <https://doi.org/10.1145/1778765.1778786>
- Chris Wojtan, Nils Thürey, Markus Gross, and Greg Turk. 2009. Deforming Meshes That Split and Merge. *ACM Transactions on Graphics (Proc. of SIGGRAPH 2009)* 28, 3 (2009), 76:1–10. <https://doi.org/10.1145/1531326.1531382>
- Chris Wojtan and Greg Turk. 2008. Fast Viscoelastic Behavior with Thin Features. *ACM Transactions on Graphics (Proc. of SIGGRAPH 2008)* 27, 3 (2008), 47:1–8. <https://doi.org/10.1145/1360612.1360646>
- Joel Wretborn, Rickard Armiendo, and Ken Museth. 2017. Animation of Crack Propagation by Means of an Extended Multi-body Solver for the Material Point Method. *Computers and Graphics* 69, C (2017), 131–139. <https://doi.org/10.1016/j.cag.2017.10.005>
- Xiao Yan, Yun-Tao Jiang, Chen-Feng Li, Ralph R. Martin, and Shi-Min Hu. 2016. Multiphase SPH Simulation for Interactive Fluids and Solids. *ACM Transactions on Graphics (Proc. of SIGGRAPH 2016)* 35, 4 (2016), 79:1–11. <https://doi.org/10.1145/2897824.2925897>
- Xiao Yan, Chen-Feng Li, Xiao-Song Chen, and Shi-Min Hu. 2018. MPM simulation of interacting fluids and solids. *Computer Graphics Forum* 37, 8 (2018), 183–193. <https://doi.org/10.1111/cgf.13523>
- Tao Yang, Jian Chang, Ming C. Lin, Ralph R. Martin, Jian J. Zhang, and Shi-Min Hu. 2017. A Unified Particle System Framework for Multi-phase, Multi-material Visual Simulations. *ACM Transactions on Graphics (Proc. of SIGGRAPH Asia 2017)* 36, 6 (2017), 224:1–13. <https://doi.org/10.1145/3130800.3130882>
- Tao Yang, Jian Chang, Bo Ren, Ming C. Lin, Jian Jun Zhang, and Shi-Min Hu. 2015. Fast Multiple-fluid Simulation Using Helmholtz Free Energy. *ACM Transactions on Graphics (Proc. SIGGRAPH Asia 2015)* 34, 6 (2015), 201:1–11. <https://doi.org/10.1145/2816795.2818117>
- Tao Yang, Ralph R. Martin, Ming C. Lin, Jian Chang, and Shi-Min Hu. 2017. Pairwise Force SPH Model for Real-Time Multi-Interaction Applications. *IEEE Transactions on Visualization and Computer Graphics* 23, 10 (2017), 2235–2247. <https://doi.org/10.1109/TVCG.2017.2706289>
- Kenji Yasuda. 1979. *Investigation of the analogies between viscometric and linear viscoelastic properties of polystyrene fluids*. dissertation. Massachusetts Institute of Technology. <https://dspace.mit.edu/handle/1721.1/16043>
- Yonghao Yue, Breannan Smith, Christopher Batty, Changxi Zheng, and Eitan Grinspun. 2015. Continuum Foam: A Material Point Method for Shear-Dependent Flows. *ACM Transactions on Graphics* 34, 5 (2015), 160:1–20.
- Yonghao Yue, Breannan Smith, Peter Yichen Chen, Maytee Chantha Rayukhonthorn, Ken Kamrin, and Eitan Grinspun. 2018. Hybrid grains: adaptive coupling of discrete and continuum simulations of granular media. *ACM Transactions on Graphics (Proc. of SIGGRAPH Asia 2018)* 37, 6 (2018), 283:1–19.
- Boris Zhusub. 2014. Viscosity Blending Equations. *Lube Magazine* 121 (2014), 22–27.
- Bo Zhu, Minjae Lee, Ed Quigley, and Ronald Fedkiw. 2015. Codimensional non-Newtonian Fluids. *ACM Transactions on Graphics (Proc. of SIGGRAPH 2015)* 34, 4 (2015), 115:1–9. <https://doi.org/10.1145/2766981>
- Fei Zhu, Jing Zhao, Sheng Li, Yong Tang, and Guoping Wang. 2017. Dynamically Enriched MPM for Invertible Elasticity. *Computer Graphics Forum* 36, 6 (2017), 381–392. <https://doi.org/10.1111/cgf.12987>
- Yongning Zhu and Robert Bridson. 2005. Animating Sand As A Fluid. *ACM Transactions on Graphics (Proc. of SIGGRAPH 2005)* 24, 3 (2005), 965–972. <https://doi.org/10.1145/1073204.1073298>

## A PROOF OF THEOREM 4.1

**PROOF.** Suppose that we mix  $A$  and  $B$  with the mass ratio  $\alpha_1 : 1 - \alpha_1$  to produce  $C$ , and with the ratio  $\alpha_2 : 1 - \alpha_2$  to produce  $D$ . Then, we mix  $C$  and  $D$  with the ratio  $\zeta : 1 - \zeta$  to produce  $E$ . Alternatively,  $E$  can be directly produced from  $A$  and  $B$  with the ratio  $\zeta\alpha_1 + (1 - \zeta)\alpha_2 : 1 - \zeta\alpha_1 - (1 - \zeta)\alpha_2$ . Assuming that we can write  $\tilde{\Phi}(\alpha) = \Phi(\alpha; \beta)$ , we have the viscosities  $\eta_C$  and  $\eta_D$  for  $C$  and  $D$ , respectively, according to (27):

$$F(\eta_C) = \tilde{\Phi}(\alpha_1)F(\eta_A) + (1 - \tilde{\Phi}(\alpha_1))F(\eta_B), \quad (45)$$

$$F(\eta_D) = \tilde{\Phi}(\alpha_2)F(\eta_A) + (1 - \tilde{\Phi}(\alpha_2))F(\eta_B); \quad (46)$$

thus, we have the viscosity  $\eta_E$  for  $E$  as a blend of  $C$  and  $D$ :

$$\begin{aligned} F(\eta_E) &= \tilde{\Phi}(\zeta)F(\eta_C) + (1 - \tilde{\Phi}(\zeta))F(\eta_D) \\ &= \left( \tilde{\Phi}(\zeta)\tilde{\Phi}(\alpha_1) + (1 - \tilde{\Phi}(\zeta))\tilde{\Phi}(\alpha_2) \right) F(\eta_A) \\ &\quad + \left( \tilde{\Phi}(\zeta)(1 - \tilde{\Phi}(\alpha_1)) + (1 - \tilde{\Phi}(\zeta))(1 - \tilde{\Phi}(\alpha_2)) \right) F(\eta_B). \end{aligned} \quad (47)$$

On the other hand, from the direct blending of  $A$  and  $B$ , we know that  $\eta_E$  should also satisfy

$$F(\eta_E) = \tilde{\Phi}(\zeta\alpha_1 + (1 - \zeta)\alpha_2)F(\eta_A) + (1 - \tilde{\Phi}(\zeta\alpha_1 + (1 - \zeta)\alpha_2))F(\eta_B). \quad (48)$$

Relating (47) and (48), and noticing that the above relation must hold for an arbitrary valid choice of  $\eta_A$  and  $\eta_B$ , the coefficients of  $F(\eta_A)$  and  $F(\eta_B)$  in (47) and (48) must coincide, so we must have

$$\tilde{\Phi}(\zeta\alpha_1 + (1 - \zeta)\alpha_2) = \tilde{\Phi}(\zeta)\tilde{\Phi}(\alpha_1) + (1 - \tilde{\Phi}(\zeta))\tilde{\Phi}(\alpha_2) \quad (49)$$

From the *zero law*, we notice that  $\tilde{\Phi}(0) = 0$  and  $\tilde{\Phi}(1) = 1$  must hold. Then, considering the case  $\alpha_2 = 0$ , we have the *product decomposition rule*:

$$\tilde{\Phi}(\zeta\alpha_1) = \tilde{\Phi}(\zeta)\tilde{\Phi}(\alpha_1). \quad (50)$$

Next, considering the case  $\alpha_1 = 0$  and using (50), we have

$$\begin{aligned}(1 - \tilde{\Phi}(\zeta))\tilde{\Phi}(\alpha_2) &= \tilde{\Phi}((1 - \zeta)\alpha_2) \\ &= \tilde{\Phi}(1 - \zeta)\tilde{\Phi}(\alpha_2),\end{aligned}\quad (51)$$

and further noting that  $\tilde{\Phi}(\alpha_2)$  can be chosen such that  $\tilde{\Phi}(\alpha_2) \neq 0$ , we have the *one-minus rule*:

$$\tilde{\Phi}(1 - \zeta) = (1 - \tilde{\Phi}(\zeta)). \quad (52)$$

Finally, substituting  $\alpha_1 = \frac{x}{z}$ ,  $\zeta = z$ , and  $\alpha_2 = \frac{y}{1-z}$  into (49), we have

$$\tilde{\Phi}(x + y) = \tilde{\Phi}(z)\tilde{\Phi}\left(\frac{x}{z}\right) + (1 - \tilde{\Phi}(z))\tilde{\Phi}\left(\frac{y}{1-z}\right). \quad (53)$$

Using the relations (50) and (52), we have the *additive decomposition rule*:

$$\tilde{\Phi}(x + y) = \tilde{\Phi}(x) + \tilde{\Phi}(y). \quad (54)$$

This is the Cauchy's functional equation, and has the solution  $\tilde{\Phi}(x) = cx + d$  if we assume  $\tilde{\Phi}$  is Lebesgue measurable. We can easily verify this for a differentiable  $\tilde{\Phi}$ , by differentiating (54) with respect to  $y$ , setting  $y = 0$ , and letting  $c = \tilde{\Phi}'(0)$ . Then, we have  $\tilde{\Phi}'(x) = c$  for an arbitrary  $x$ ; thus,  $\tilde{\Phi}(x)$  must have the form  $\tilde{\Phi}(x) = cx + d$ . Since  $\tilde{\Phi}(0) = 0$  and  $\tilde{\Phi}(1) = 1$ , we conclude that  $c = 1$  and  $d = 0$ ; hence, we arrive at  $\tilde{\Phi}(\alpha) = \alpha$ .  $\square$

## B LIMITING BEHAVIOR OF $(\alpha A^p + (1 - \alpha)B^p)^{1/p}$

Let  $C^p = (\alpha A^p + (1 - \alpha)B^p)^{1/p}$ . We consider the limiting behavior of  $p \rightarrow 0$ , and show that it corresponds to multiplicative blending. We use the following identity<sup>3</sup>:

$$\lim_{p \rightarrow 0} \left( \frac{f(x + p)}{f(x)} \right)^{\frac{1}{p}} = \exp \left( \frac{f'(x)}{f(x)} \right). \quad (55)$$

We set  $f(x) = \alpha A^x + (1 - \alpha)B^x$ . We then have  $f'(x) = \alpha A^x \ln A + (1 - \alpha)B^x \ln B$ . Taking  $x = 0$ , we find that  $f(0) = 1$ , so (55) becomes

$$\lim_{p \rightarrow 0} (\alpha A^p + (1 - \alpha)B^p)^{\frac{1}{p}} = \exp(\alpha \ln A + (1 - \alpha) \ln B); \quad (56)$$

hence,

$$\ln C = \alpha \ln A + (1 - \alpha) \ln B. \quad (57)$$

<sup>3</sup>[https://en.wikipedia.org/wiki/List\\_of\\_limits](https://en.wikipedia.org/wiki/List_of_limits)